Response of Axially Loaded Piles in Sands with and without Seismically Induced Porewater Pressures

Mohamed Ashour, M. ASCE[1], Amr Helal [2]

Abstract

The paper presents a procedure to predict the mobilized shaft resistance of axially loaded piles in medium dense sands with/without liquefaction (limited liquefaction). The technique is developed to assess the load transfer-settlement (t-z) curve, and varying pile-side resistance and pile-head axial load versus the pile settlement in sands. The mobilized pile-side and tip resistances are determined based on stress-strain relationships of sands under drained and undrained conditions. The proposed approach allows the assessment of the t–z curve along the pile length under undrained conditions with the consideration of the porewater pressure (PWP) developing in surrounding sands. The presented model accounts for the variation of the PWP in the near-field soil under axial load which is combined with the influence of the free-field PWP generated by cyclic loading (post-seismic event). The study also employs an undrained constitutive model for sands with limited liquefaction to calculate the variation of shear stresses and strains in the surrounding soil along the length of the pile. A computer code is developed to implement the presented technique.

Keywords**:** Pile, shaft resistance; axial load; sand, liquefaction; t-z curve.

[1] Associate Professor, Dept. of Civil and Environmental Engineering, University of Alabama in Huntsville, USA
Email: ashour@eng.uah.edu, and Associate Professor, College of Engineering, Mansuora University, Egypt
Tel.: +1 256 824 5029; Fax: +1 256 824 6724.
[2]Graduate Research Assistant, Dept. of Civil and Environmental Engineering, University of Alabama in Huntsville,

Introduction

Piles in cohesionless soil gain their support from the tip resistance and transfer of axial load via the pile wall/shaft resistance along its length. The contribution of pile shaft resistance to the axial load carried by the pile proportionally increases with pile embedded length. It should be noted that both pile tip and skin resistance are interdependent. The estimation of the pile axial capacity relies heavily on empirical correlations. The pile shaft resistance is influenced by the state and properties of soils within the critical zone immediately surrounding the pile. In addition, the method utilized for driving the pile, the roughness of the pile surface (i.e. pile materials) and the state of the pile end (closed/open end) have their influence on the pile shaft resistance. Furthermore, in reality, soil profiles often consist of multiple layers of soils that may contain sand, clay and silt. The technique presented by Ashour et al. (2009) for axially loaded piles in clay is combined with the current procedure to analyze the axially loaded piles in sand and clay soil deposits.

The assessment of the mobilized load transfer of a pile in sand depends on the success in developing a representative (t-z) relationship. This can be achieved via empirical relationships or numerical methods. The load transfer-settlement (t-z) curve method is the most widely used technique to compute the response of axially loaded piles, and is particularly useful when the soil behavior is clearly nonlinear and/or when the soil surrounding the pile is stratified. This method involves modeling the pile as a series of elements (segments) supported by discrete nonlinear springs, which represent the soil-pile skin friction (t-z springs), along with a nonlinear pile tip (end - bearing) Q_p-z_p spring. Building on this work and based on additional empirical results, general recommendations for estimating t-z and Q_p-z_p curves for axially loaded piles in sands have been proposed by Vijayvergiya (1977), API (1993), Altaee et al.(1992), Alawneh et al.(2001) and Seo et al. (2009).

t-z curves can also be constructed satisfactorily using a theoretical approach related to the shear stiffness of the soil surrounding the pile. Several methodologies to develop theoretically based load transfer curves have been proposed e.g., Kraft, et al. (1981); Chow (1986); McVay et al. (1989) and Randolph (1994).

Salgado et al. (2011) presented a mathematical formulation to perform a load-settlement analysis for a pile with circular cross section installed in multilayered elastic soil that accounts for both vertical and radial soil displacements. The analysis follows from the solution of the differential equations governing the displacements of the pile–soil system obtained using variational principles. The method is extension for the method of Seo and Prezzi (2007), which considers only vertical soil displacement.

API (1993) recommends the use of empirical t-z curve for sands assuming the mobilized unit side shear stress (τ) to change linearly with the pile segment displacement (z) till τ reaches its maximum value (τ_{max}) at z_c = 0.25 mm. Vijayvergiya (1977) suggested an empirical nonlinear formula similar to the API one to calculate τ as a function of z_c. Hoit et al. (2007) presented a study on the assessment of the t-z curves in sand based on the API recommendations which are also employed in some design software packages.

Coyle and Castello (1981) proposed design correlations for piles in sand using δ average that was assumed equal to the residual angle of shearing resistance of the sand friction angle (φ). Randolph and Wroth (1978) presented approximate analytical solution for analysis of settlement of single pile using theoretical formulations for 1) linear degradation of the shear stress (τ) and displacement in the surrounding soil with the radial distance (r) as a function of the shear stress at the pile-soil interface (τ_o) and pile radius r_o (i.e. $\tau = \tau_o\, r_o/r$); 2) a constant shear displacement zone of influence (r_m) along the length of the pile (L) where the soil shear modulus at L/2 and pile tip are linked via a constant ratio (ρ). By knowing L, r_o, and r_m, Randolph and Wroth (1978) developed the following equation to calculate the t-z curve as a function of a constant G assuming a linear elastic soil.

$$z = \frac{\tau_o\, r_o}{G} \ln\left(\frac{r_m}{r_o}\right) \tag{1}$$

Where $r_m = 2.5\, L\, \rho\, (1 - \nu)$ and ν = Poisson's ratio. Kraft et al. (1981) used the work done by Randolph and Wroth (1978) to develop an equation for the t-z curve using a hyperbolic stress-strain relationship based on the initial shear modulus of sand (G_i).

$$G = G_i \left[1 - \frac{\tau_o R_f}{\tau_{max}}\right]^2 = G_i \left[1 - \psi\right]^2 \tag{2}$$

$$z = \frac{\tau_o\, r_o}{G_i} \ln\left[\left(\frac{r_m}{r_o} - \psi\right) / \left(1 - \psi\right)\right] \tag{3}$$

R_f = stress-strain curve fitting constant, and τ_{max} is the maximum shear stress at failure. Zhu and Chang (2002) used modified hyperbolic models to assess the t-z curve. Instead of using a hyperbolic stress-strain relationship, Armaleh and Desai (1987) used Ramber-Osgood model to assess the t-z curve in sands.

The semi-empirical procedure presented in this paper for axially loaded piles utilizes the stress-strain relationship of sand (Norris 1986 and Ashour et al. 1998) to obtain the t-z curve and pile shaft resistance in sand. The method of slices utilized in this technique determines the degradation of shear stress/strain and vertical displacement within the vicinity of the axially loaded pile under drained static conditions (pre-earthquake). As a result, the t-z curves and the variation of side resistance along the pile length can be assessed using a combination of tip and side resistance/displacement of the pile and associated pile elastic deformation. The presented pre-earthquake (i.e. drained) model shows the radial degradation of the shear stress (τ) and strain (γ) in the sand critical zone around the pile starting from the soil-pile interface. In reality, it is recognized that mobilizing the shaft resistance requires very small movements, whereas mobilizing an ultimate toe resistance requires many times larger movement (Fellenius 1999).

The undrained stress-strain model of sands with limited liquefaction (Ashour et al. 2009) is employed to assess the t-z curve and skin resistance for the pile length into partially liquefied sand layers where the excess water pressure ratio (r_u) is less than 1 along with the pile-head load settlement curve. Such a scenario of soil limited liquefaction is common to occur with medium dense sands (Dr = 35% - 65%). It should be noted that the t-z curve is determined based on the mobilized tip and side resistance/displacement of the pile and associated pile elastic deformation. The pile tip in the presented study is embedded into a non-liquefiable soil layer (such as clay or dense sand). The presented model relies on the ability to develop and utilize pre- and post-limited liquefaction stress-strain relationship with drained and undrained conditions (i.e. considering the effect of varying far/free- and near-field porewater pressure $u_{xs,ff}$ and $u_{xs,nf}$, respectively). The development of full and limited liquefaction in the same sand stratum depends on the characteristics of the regional seismic activities (i.e. the magnitude of the earthquake M and the peak ground acceleration a_{max}).

Piles in liquefiable soils and failure mechanisms

Because of the combination of axial and lateral loading on piles during or post a seismic event as a result of superstructure inertial force and/or lateral soil spreading, respectively, the influence of the axial load (P) in association with lateral loads (i.e. pile deflection, Δ) is dominated via the excessive moment caused by P-Δ effect combined with lateral forces (Fig. 1c) with/without lateral spreading (Maheshwari and Sarkar 2011, Haldar and Babu 2010, Ashour and ardalan 2011). While some focus has been given to the piles in fully liquefied soil layer(s) under axial loading as a source of pile buckling instability (Fig. 1a) (Bhattacharya et al. 2005, Shanker et al. 2007, and Haldar and Babu 2010), no attention has been given to the axially loaded piles in soils with limited liquefaction (Fig. 1b) that could develop in medium dense sands (Dr = 35% – 65%) especially with moderate seismic events. For axially loaded pile segments embedded into liquefiable soil layers, current design procedures assume no sand resistance or reduced sand residual strength (American Association of State Highway and Transportation Officials, AASHTO, 2007) based on the free-field liquefaction potential with no consideration for developing near-field PWP. On the other side, some researchers have focused on the negative skin friction (Yao et al. 2012) and downdrag effect on the pile axial resistance that could take hours/days after liquefaction to develop according to the site geotechnical conditions (Fellenius and Siegel 2008 and Rollins and Strand 2006).

The paper studies the post-limited liquefaction loading scenario immediately after the end of the seismic event (i.e. superstructure inertial force = 0) in level ground (i.e. no possibility of lateral soil spreading to occur) where the axial load dominates the behavior of the pile. The paper highlights the drop in sand shear strength (medium dense sand) in response to the earthquake induced porewater pressure $u_{xs,ff}$ with $r_u < 1$ generating a state of limited soil liquefaction in the free-field that is associated with pile axial loading and related near-filed porewater pressure, $u_{xs,nf}$ (Fig. 2). The presented model assumes undrained conditions with no water pressure dissipation (i.e. no sand volume change) during a short period of time (few minutes) after the earthquake which is a common scenario that could happen due to the presence of clay layer or soil deposit with low permeability (more fines) above the liquefied sand layer.

Partially liquefied sand in the near-field of axially loaded pile experiences more degradation in its undrained strength (σ_d) due to the buildup of the excess PWP (Fig. 2). The soil experiences developing (partial or limited) liquefaction in the free-field if r_u induced by the earthquake shaking (i.e. $u_{xs,ff}$) is less than 1, and full liquefaction if r_u = 1. The axial load from the superstructure induces additional near-field porewater pressure, $u_{xs,nf}$, that may be either positive or negative changes superposed onto $u_{xs,ff}$.

Immediately after the earthquake and the presence of considerable axial loads, two possible pile failure mechanisms are anticipated to accompany the development of full liquefaction in level ground. Slender piles could be subjected to buckling instability if sufficient length of the pile becomes unsupported by forming a plastic hinge. The other failure mechanism would be an excessive pile settlement due to the loss of all or part of the shaft resistance and having most of the axial load carried by the pile tip. Therefore, designers always look for a firm and non-liquefiable soil deposit (stiff clay, dense sand or rock) in which the pile tip is embedded in order to reduce any excessive pile settlement (i.e. bearing failure). In the case of having the pile tip embedded into a liquefiable soil, soil improvement such as soil grouting needs to be considered. This paper studies the behavior of pile under axial load where a significant length of the pile penetrates a sand layer(s) with limited liquefaction and the pile tip is embedded in non-liquefiable soil layer (dense sand or clay) where the pile is still subjected to excessive settlement due to the degradation in sand strength. Settlement will continue until sufficient base capacity and shaft friction is mobilized to bring the axial load on the pile into equilibrium.

Load transfer–settlement model (t-z) of sands (no liquefaction)

The methodology presented models the soil around the pile/shaft segment (H_s) at depth x as soil slices (1, 2, 3 ….m+n) that deform vertically as shown in Figs. 3a and 3b. H_s can be assumed equal to the pile diameter (D). The shear stress/strain caused by the shaft settlement (z) at a particular depth gradually decreases along the radial distance (r) from the pile wall. As seen in Fig. 3c, the shear stress (τ), settlement z (i.e. soil shear strain γ) experience their largest values (τ_o, z_o and γ_o) for a particular load increment at the soil-pile interface where $r = r_o$. Kraft et al. (1981) showed that the actual radial degradation of shear stress and displacement in sand vicinity around the pile take a parabolic decreasing pattern. The suggested model assumes a nonlinear parabolic degradation for the soil vertical displacement (z) versus the radial distance (r).

$$z = z_o \left(\frac{r_o}{r} \right)^2 \tag{4}$$

Where r is the radial distance of the point of question, and $z = z_o$ at $r = r_o$. The pattern of radial variation of soil vertical displacement (in Eqn. 4) is assumed based on the experimental data observed by Robinsky and Morrison (1964) and the analysis presented by Seo et al. (2008) and Chow (2007), which is also in agreement with soil displacement nonlinear degradation pattern obtained from the Finite Element (FE) Program (PLAXIS) using the hardening soil model with soil's stiffness E_{50} of 42000 kN/m2 (Fig. 4). However, the experimental data (i.e. Eqn. 1) displays rapid degradation for soil displacement compared to the FE method results.

Isotropic conditions are assumed in sands after pile installation and horizontal (confining) stress is equal to the vertical effective overburden, $\bar{\sigma}_{vo}$ (i.e. lateral earth pressure coefficient K = 1 and $\bar{\sigma}_{3c} = \bar{\sigma}_{vo}$ before loading), as shown in Fig. 5. The shear strain associated to soil vertical displacement in a sand slice i between r_i and r_{i+1} (Fig. 3b) is determined as

$$\gamma_i = \frac{z_i - z_{i+1}}{r_{i+1} - r_i} = \frac{\Delta z_i}{\Delta r_i} \tag{5}$$

Δr_i has smaller values close to the pile wall that increase away from the pile (Fig. 3a). The pile axial load is increasing gradually (incrementally) to produce larger shear stress (τ_o) and strain at the soil-pile interface (Fig. 5). The pile settlement at depth (x) is accompanied by τ_o at the soil-pile interface and Mohr circle of a radius τ_o and confining pressure $\bar{\sigma}_3$.

As shown in Fig. 5, the progress in the axial load produces larger Mohr circles with larger values of τ_o and decreasing values for $\bar{\sigma}_3$ till $\tau_o = \tau_{max}$ when the mobilized friction angle (φ_m) in the sand becomes equal to the soil-pile friction angle (δ). Figure 3c demonstrates the degradation of shear stress at the soil-pile interface τ_o (caused by pile settlement z) with radial distance r till τ and z become equal to zero at a large value of r.

The constitutive model for drained soil presented by Ashour et al. (1998) (Fig. 6) is employed to determine the associated normal and shear strains ε and γ, respectively.

$$\gamma = \varepsilon\,(1 + \nu) \tag{6}$$

$$SL = \frac{\sigma_d}{\sigma_{df}} = \frac{2\tau}{\sigma_{df}} \tag{7}$$

The Poisson's ratio ν is assumed to change from 0.1 to 0.5 as a function of the stress level in soil (SL),

$$\nu = 0.1 + 0.4\,SL \tag{8}$$

and

$$\sigma_{df} = \overline{\sigma}_3 \left[\tan^2\left(45 + \frac{\varphi}{2} \right) - 1 \right] \tag{9}$$

For a specific pile settlement z_o at depth x, a mobilized value of τ_o (Fig. 5) is assumed to calculate the associated confining pressure $\overline{\sigma}_3$, SL, ε_o and γ_o at the soil-pile interface using the constitutive model in Fig. 6 and Eqns. 6 through 9. The radial degradation in γ (Eqns. 4 and 5) is used to sum up the radial developing settlement Δz_i in each soil slice where $z_o = \Sigma\, \Delta z_i$. It should be noticed that $\overline{\sigma}_3$ and τ vary for each slice due to the radial degradation of τ_o. τ_o is adjusted for the pile segment in question till calculated z_o converges properly to z_o of the pile segment obtained from the global iterative stability analysis of the pile side and tip resistance model shown in Fig. 7.

Figure 8 presents the radial variation of shear stress and strain and pile segment displacement at 6 m depth below ground surface for a 0.305-m diameter steel pipe pile embedded 15 m into medium dense sand (angle of internal friction φ = 35, effective unit weight $\overline{\gamma}$ = 9 kN/m^3). The shear stress/strain and displacement are also calculated at depth 6m below the ground surface for the same axial pile-head load (Q = 222 kN).

Figure 9 also shows the shear modulus degradation curve (G/G_i vs. shear strain) obtained from the utilized soil model where G is calculated as a function of varying values of E and ν at the soil-pile interface.

$$G = \frac{E}{2(1+\nu)} \tag{10}$$

In comparison with the ultimate side frictional resistance (f_s) obtained from the MTD method (Jardine and Chow 1996 and Randolph 2003), Fig. 10 reflects the proposed technique capability of predicting the nonlinear variation of the mobilized f_s along the pile length under progressing pile-head axial load (Q) in association with the pile tip resistance (Q_p). The 1-m diameter open ended steel pipe pile is embedded 40 m in medium dense sand with φ = 35 and $\bar{\gamma}$ = 11 kPa. The MTD method presented in Fig. 10 is derived from the Imperial College field studies and database.

Pile tip (point) resistance and settlement (Q_p – z_p) in sand

It is evident that the associated pile tip resistance manipulates the side resistance of the pile shaft. As presented in the analysis procedure, the pile tip resistance should be assumed at the first step. As a result, the shear resistance and displacement of the upper segments of the pile can be computed based on the assumed pile tip movement. This indicates the need for a practical technique that allows the assessment of the pile tip load-displacement relationship under a mobilized or developing state. It should be emphasized that the presented procedure has the advantage of utilizing the same stress-strain model of sand (Fig. 6) to determine the mobilized resistance and associated settlement at the pile tip and along the side of the pile.

In association with the pile side shear resistance model presented in this study, the approach established by Elfass (2001) is employed to compute the pile tip load-settlement in sand. The failure mechanism model assumes four failure zones represented by four Mohr circles, as shown in Fig. 11. This mechanism yields the bearing capacity (q) and its relationship with the deviatoric stress (σ_d) of the last (fourth Mohr circle) as shown in Fig 11.

$$\sigma_d = 0.6\,q \tag{11}$$

The pile tip resistance (Q_P) is given as,

$$Q_P \;=\; q\,A_{base} = \frac{\sigma_d}{0.6}A_{base} \qquad (12)$$

where A_{base} is the cross sectional area of the pile tip.

As seen in Fig. 11, the Mohr Columb strength envelope is nonlinear and requires the evaluation of the secant angle of the fourth circle (φ_{IV}) tangent to the curvilinear envelope. The angle of the secant line tangent to first circle (φ_I) at effective overburden pressure can be obtained from the field blow data count (SPT test) or a laboratory triaxial test at approximately 100 kPa (1 tsf) confining pressure. Due to the increase in the confining pressure $(\bar{\sigma}_3)$ from one circle to the next, the friction angle (φ) decreases from φ_I at $(\bar{\sigma}_3)_I$ to φ_{IV} at $(\bar{\sigma}_3)_{IV}$ assuming a value for $\Delta\varphi$ where

$$\varphi_{IV} = \varphi_I - \Delta\varphi \qquad (13)$$

Based on the following Bolton (1986) relationship modified by Elfass (2001) as shown in Fig. 12

$$\varphi_{peak} \;=\; \varphi_{\min} + \varphi_{diff} \qquad (14)$$

$$\varphi_{diff} \;=\; 3I_R \;=\; 3D_R\left\{10 - \ln\left[\left(\frac{2+\tan^2(45+\varphi/2)}{3}\right)\bar{\sigma}_3\right]\right\} \;-\; 1 \qquad (15)$$

$\bar{\sigma}_3$ is in kPa and φ_{min} is the lowest friction angle that φ may reach at high confining pressure, and Dr is used as decimal value. Knowing the sand relative density (Dr) and associated friction angle under original confining pressure $(\bar{\sigma}_3 = \bar{\sigma}_{vo})$, Eqn. 15 can be used to calculate the reduction in the friction angle $\Delta\varphi$ due to the increase of the confining pressure from $\bar{\sigma}_{vo}$ to $(\bar{\sigma}_3)_{IV}$ and the associated decrease of the friction angle from φ_I to φ_{IV}. Assume a reduction ($\Delta\varphi$

= 3 or 4 degrees) in the sand friction angle at $(\bar{\sigma}_3 = \bar{\sigma}_{vo})$ due to the increase in the confining pressure from $\bar{\sigma}_{vo}$ to $(\bar{\sigma}_3)_{IV}$, as seen in Fig. 12. Therefore,

$$\Delta\varphi = (\varphi_{diff})_I - (\varphi_{diff})_{IV} \tag{16}$$

But the friction angle φ_{IV} associated with $(\bar{\sigma}_3)_{IV}$ can be also calculated as

$$\varphi_{IV} = \varphi_I - \Delta\varphi \log \frac{(\bar{\sigma}_3)_{IV}}{\bar{\sigma}_{vo}} \tag{17}$$

Compare the assumed value of φ_{IV} with the value obtained in Eqn. 13. If they are different, adjust for new value and repeat the process (Eqn. 13 through 17) until the value of φ_{IV} converges and the difference in $\Delta\varphi$ calculated yields to the targeted tolerance.

Using the deviatoric stress (σ_d) of the fourth circle,

$$\sigma_{df} = (\bar{\sigma}_3)_{IV}\left(\tan^2(45+\varphi_{IV}/2)-1\right) \tag{18}$$

Where

$$(\bar{\sigma}_3)_{IV} = \bar{\sigma}_{vo} + q - \sigma_d = \bar{\sigma}_{vo} + 0.4q \tag{19}$$

The current stress level (SL) in soil (Zone 4 below pile tip) is evaluated as

$$SL = \frac{\tan^2(45+\varphi_m/2)-1}{\tan^2(45+\varphi_{IV}/2)-1} = \frac{\sigma_d}{\sigma_{df}} \quad ; \quad \sigma_d = SL\,\sigma_{df} \tag{20}$$

Where

$$\varphi_m = \sin^{-1}\left(\frac{\sigma_d/2}{(\bar{\sigma}_3)_{IV} + \sigma_d/2}\right) \tag{21}$$

Pile tip settlement

The pile tip displacement in sand can be determined based on the drained stress-strain relationship presented in Fig. 6 where the soils strain (ε) below the pile tip is evaluated according to the model shown in Fig. 13.

For a constant Young's modulus (E) with depth, the strain or ε_1 profile has the same shape as the elastic ($\Delta\sigma_1$ - $\Delta\sigma_3$) variation or Schmertmann's I_z factor (Schnertmann 1970, Schnertmann et al. 1979 and Norris 1986). Taking ε_1 at depth r_o below the pile tip (the peak of the I_z curve), the pile tip displacement (z_P) is a function of the area of the triangular variation (Fig. 13).

$$z_P = 2 \varepsilon r_o \tag{22}$$

where r_o is the radius of the pile tip. Dealing with different values for pile tip resistance (Eqn. 12), the associated deviatoric stress (Eqn. 11), stress level (Eqn. 19) and principal strain (ε) (Fig. 6) can be used to assess the tip movement in order to construct the pile tip load-settlement (Q_P – z_P) curve.

Constitutive modeling of saturated sands with limited liquefaction

The undrained stress-strain model of sands with limited liquefaction (i.e. $r_u < 1$) as developed by Ashour et al. (2009) is employed in the current analysis. As presented experimentally by several researchers, the undrained response of sands with limited liquefaction under monotonic loading may experience initial (restrained) contractive behavior that is then followed by dilative behavior in response to a drop in the confining pressure ($\overline{\sigma}_3 > 0$) (Fig. 2).

The assessed value of r_u in the free-field (i.e. Δu_c) induced by the earthquake is obtained using the procedures presented by Idriss and Boulanger (2004) for calculating the magnitude scaling factor and liquefaction potential based on SPT-N. Under monotonic loading, the undrained behavior of sand with limited liquefaction induced by cyclic loading (i.e. $r_u < 1$ and $\overline{\sigma}_3 = \overline{\sigma}_{3cc} >$

0 at point r) reflects initial restrained contractive behavior followed by dilative response (at point s) whereby its effective stress path ($\bar{p} = \bar{\sigma}_3 + \sigma_d / 2$) reaches the failure line and thereafter marches up the failure line due to restrained dilative (Fig. 14b).

The technique presented by Ashour et al. (2009) allows assessment of the undrained stress-strain behavior of sand with limited liquefaction based on drained test behavior. Such assessment requires only basic properties of the sand such as its relative density [or $(N_1)_{60}$], effective angle of internal friction (φ), roundness of the sand grains (ρ), drained axial strain at 50% stress level (ε_{50}), and confining pressure ($\bar{\sigma}_3$). ε_{50} can be obtained from the conventional triaxial test or the chart developed by Norris (1986) and also presented by Ashour et al. (1998) which is a function of the sand uniformity coefficient (C_u) and void ratio (e).

The experimental basis of the utilized technique employs a series of drained tests, with volume change measurements, on samples isotropically consolidated to the same confining pressure, $\bar{\sigma}_{3c}$, and void ratio, e_c, to which the undrained test is to be subjected. However, the drained tests are rebounded to different lower values of effective confining pressure, $\bar{\sigma}_3$, before being sheared. Such a technique allows the assessment of undrained behavior of sand isotropically consolidated to $\bar{\sigma}_{3c}$ that is subjected to compressive monotonic loading (Norris et al. 1997 and Ashour and Norris 1999). During an isotopically consolidated undrained (ICU) test, the application of a deviatoric stress, σ_d, in compressive monotonic loading causes additional PWP, Δu_d, that results in lower effective confining pressure, $\bar{\sigma}_3$, i.e.

$$\bar{\sigma}_3 = \bar{\sigma}_{3c} - \Delta u_d \quad \text{(No cyclic loading)} \qquad (23)$$

And an associated isotropic expansive volumetric strain, $\varepsilon_{v,iso}$, the same as recorded in an isotropically rebounded drained triaxial test (prior to shear loading). However, in the undrained test, the volumetric change or volumetric strain must be zero. Therefore, there must be a compressive volumetric strain component, $\varepsilon_{v,\ shear}$, due to the deviatoric stress, σ_d. This shear induced volumetric strain, $\varepsilon_{v,\ shear}$, must be equal and opposite to $\varepsilon_{v,\ iso}$, so that the total volumetric strain, $\varepsilon_v = \varepsilon_{v,\ iso} + \varepsilon_{v,\ shear}$, in undrained response is zero, or $\varepsilon_{v,\ shear} = -\varepsilon_{v,iso}$. In the isotropically rebounded drained shear test, $\varepsilon_{v,iso}$ and then $\varepsilon_{v,shear}$ (to match $\varepsilon_{v,\ iso}$) are obtained separately and sequentially in the undrained test, they occur simultaneously.

Ashour et al. (2009) extended the technique to incorporate the excess PWP induced by cyclic loading (Δu_c) and its influence on the undrained behavior of sands under the compressive monotonic loading (Δu_d) when the sand is subjected to limited liquefaction.

$$\bar{\sigma}_3 = \bar{\sigma}_{3c} - u_{xs} = \bar{\sigma}_{3c} - \Delta u_c - \Delta u_d = \bar{\sigma}_{3cc} - \Delta u_d \qquad (\bar{\sigma}_{3cc} > 0 \text{ and } r_u < 1) \quad (24)$$

where $\bar{\sigma}_{3cc}$ is the post-cyclic effective confining stress and $\bar{\sigma}_{3cc} = \bar{\sigma}_{3c} - \Delta u_c$. Sand is subjected to limited liquefaction if $\Delta u_c < \bar{\sigma}_{3c}$ (Fig. 14a and 14b). In order to establish undrained behavior from drained response, it is necessary to characterize the drained volume change due to shear of Fig. 14c that must be equal and opposite to the isotropic volume change due to the change in effective confining pressure ($\bar{\sigma}_3$) indicated in Fig. 14a.

The above procedure can be applied as long r_u induced by cyclic loading is less than 1 and the residual confining pressure ($\bar{\sigma}_3$) is greater than zero at point r (soil with limited liquefaction). Under monotonic loading, sand with limited liquefaction may experience a contractive response associated with a reduction in $\bar{\sigma}_3$ (to point s in Figs. 14.a and 14b) to reach the lowest value of $\bar{\sigma}_3$ (point 6 in Figs. 14b and 14c), and then rebound (dilate) with increasing $\bar{\sigma}_3$ until $\bar{\sigma}_3 = \bar{\sigma}_{3cc}$ again (point $\bar{r}$ in Figs. 14a and 14b). Sand continues to dilate beyond $\bar{\sigma}_{3cc}$ ($\bar{r}$ - $\bar{s}$, Fig. 14a) with increasing $\bar{\sigma}_3$ and monotonically induced porewater pressure (Δu_d). When $\bar{\sigma}_3$ <

$\bar{\sigma}_{3cc}$, $\varepsilon_{v,iso}$ rebounds to point s and then recompresses. This is associated with an equal net compressive $\varepsilon_{v,shear}$. However, when $\bar{\sigma}_3 > \bar{\sigma}_{3cc}$, $\varepsilon_{v,\,iso}$ moves from $\bar{r}$ to $\bar{s}$ and an equal dilative $\varepsilon_{v,shear}$ develops simultaneously.

The undrained shear strength and deviatoric stress of partially liquefied sand at any particular increment of loading is a function of the associated effective confining stress $\bar{\sigma}_3$ and stress level (SL).

$$\tau = \sigma_d / 2 = \frac{SL\ \bar{\sigma}_3}{2}\left[\tan^2\left(45 + \frac{\varphi}{2}\right) - 1\right] \tag{25}$$

The varying SL is a function of the drained ε_1, ε_{50}, and current $\bar{\sigma}_3$ and calculated as presented in Fig. 6. The presented work focuses on the undrained behavior of liquefiable sands pre- and post-peak where contractive and dilative behavior continues without reaching the steady state deformation ($d\varepsilon_v / d\varepsilon_1 = 0$) at very large soil strain.

Figure 15 shows a comparison between computed and measured response (undrained stress strain) of Fraser River and Ottawa sands (Vaid and Thomas 1995 and Castro 1969). Both sands were subjected to cyclic loading that developed free-field PWP with $r_u < 1$ before the monotonic load is applied. Input data used in the analysis is presented in the figure.

Load transfer–settlement modeling (t-z curve) in sand with limited liquefaction

Experiments by Robinsky and Morrison (1964) showed that the soil displacement pattern adjacent to a vertically loaded pile within a zone of $r_o/2$ wide adjacent to the pile accounts for 75% of the shear displacement (z) as shown in Fig. 4. An average soil strain γ_{ave} can be expressed as

$$\gamma_{ave} = \frac{0.75\,z}{r_o/2} = \frac{1.5\,z}{r_o} \tag{26}$$

γ_{ave} is employed in the current study. The undrained normal strain in the sand is expressed as

$$\varepsilon_1 = \frac{\gamma_{ave}}{(1+\nu)} = \frac{\gamma_{ave}}{1.5} \tag{27}$$

ε_1 is used in the undrained constitutive model of sand to determine the associated shear stress ($\tau_s = \sigma_d/2$) at the soil-pile interface. The full undrained stress-strain relationship of the liquefiable sand at any depth is governed by M and a_{max} of the anticipated earthquake and resulting $\bar{\sigma}_{3cc}$ in the free-field.

Figure 16 displays the mechanism of the simultaneous variation of PWP and associated undrained shear stress/strain in partially liquefied sand. Due to cyclic loading, $u_{xs,ff}$ (i.e. Δu_c) is generated and $\bar{\sigma}_{3c}$ (i.e. $\bar{\sigma}_{vo}$) drops to $\bar{\sigma}_{3cc}$ at point 1. As a result of axial loading, the progressing soil-pile displacement (z) in the critical zone around the pile develops γ and τ_s (points 1, 2, 3….). The increase of γ (due to pile settlement) in the near-field generates additional $u_{xs,nf}$ (i.e. Δu_d) and reduces the confining pressure $\bar{\sigma}_3$ between points 1 and 3 and associated Mohr circles, as seen in Fig. 16a. Mohr circle of the effective stress in sand in the near-field is adjusted for the change of the excess water pressure (Δu_d) and confining pressure $\bar{\sigma}_3$ induced by soil shearing in order to satisfy the equilibrium among γ, τ_s, Δu_d and $\bar{\sigma}_3$ (points/circles 1 to 3). As shown in Fig. 16a and 16b, Δu_d continues to build up with increasing γ, and decreasing $\bar{\sigma}_3$ along with slower increase of SL which is approaching its maximum unit value (SL = 1). Therefore, the sand undrained shear strength τ_s suffers a drop in its values (post-peak) between points 3 and 4.

Because of the dilative behavior of sand, Δu_d begins to decrease after reaching its largest value at point 4 that marks the lowest value of $\bar{\sigma}_3$ and τ_s. Δu_d continues to drop beyond point 4 with the progress of γ resulting in a rebound in $\bar{\sigma}_3$ and τ_s as demonstrated by Mohr circles of points 4 through 6 where Δu_d becomes zero.

The analysis presented in this paper utilizes a combination of a number of semi-empirical approaches 1) development of PWP in the free-field (Idriss and Boulanger 2004); 2) pile tip resistance and settlement in sands (Elfass 2001 and Schnertmann et al. 1979); 3) the constitutive model of drained sands presented by Ashour et al. (1998) to determine the pile side resistance in non-liquefied sands; 4) the undrained stress-strain model of partially liquefied sands (i.e. PWP in the near-field) established by Ashour et al. 2009 to calculate the pile side resistance in liquefied sands. The previously mentioned techniques are combined in the procedure presented in Fig. 7 as described by Coyle and Reese (1966). The Flowchart presented in Fig. 17 provides step-by step description for the calculation process as compiled in the computer code which is written in FORTRAN. It should be mentioned that the abovementioned process is applied at each pile segment (Fig. 7) to determine τ_s ($\tau_s = f_s$) associated to each pile segment displacement z.

Variation of PWP, confinement pressure, and shear stress/strain along the pile

A 0.305-m diameter steel pipe pile is driven into the soil profile shown in Table 1. The tip of the 15-m long pile is embedded into a sand layer overlain by a 10-m deposit of liquefiable medium dense sand (Dr = 50%). An earthquake with a magnitude M = 5.0 and peak-ground acceleration a_{max} = 0.15g has been utilized to generate $u_{xs,ff}$ with r_u less than 1 (i.e. limited liquefaction). The PWP curves are numbered for advancing pile head axial load (Q) increments shown in Table 2. The solid and dashed sets of curves shown in Fig. 18a describe the PWP (i.e. r_u) increase and decrease phase into sands around the pile, respectively. Under an axial load increment and due to the increasing effective soil pressure with depth, it can be seen in Fig. 18a that the PWP in the upper portion of the sand layer develops (solid curves) faster than deeper sand. Similar behavior can be also observed via the dashed curves when the PWP is decreasing.

Figure 18b presents the variation of soil-shaft friction (f_s or τ_s) along the pile length under growing axial load Q. τ_s is determined at the soil-pile interface through the clay, liquefied and non-liquefied sand layers. The technique presented by Ashour et a. (2009) is used to calculate f_s in the upper clay layer. The distribution of the axial load resistance (Q) along the pile length is presented in Fig. 18c. Curves 4 through 7 in Figs. 18b and 18c display limited increase in the pile axial resistance versus larger pile settlement associated with higher levels of r_u. Larger settlement with smaller increase in the axial load is attributed to the temporary drop of pile-soil frictional resistance before it rebounds with the decrease of the PWP (Figs. 18c and 18d). To show the effect of sand limited liquefaction on pile settlement under the same axial load increment Q_T = 530 kN (increment 7 in Table 2), the pile head maintains settlement of 9 mm (Fig. 18d) compared to 4 mm with the static (no liquefaction) conditions.

For the same soil-pile profile, Figure 19a shows the variation of the PWP in medium dense sand due to soil-pile displacement (z) at different depths using earthquake input data of M = 5.0 and a_{max} = 0.15g to induce limited liquefaction into the 10-m thick sand layer ($r_u < 1$) (before pile loading). The r_u curves in Fig. 19a demonstrate the influence of the contractive and dilative behavior of the medium dense sand layer under undrained conditions that is associated with an increase and then decrease of r_u with the progress of z (i.e. soil shear strain). The calculated undrained t-z curves at 4, 8 and 12 m deep below the ground surface (Fig. 19b) reflect the influence of the undrained stress-strain curve of liquefied sands (i.e. r_u) on the resulting shape of the t-z curve.

In order to show the effect of sand density on the t-z curve, a specific seismic scenario (M = 5.0 and a_{max} = 0.1g) has been used with the liquefiable sand layer using three states of sand relative density for the 10-m thick sand layer presented in Table 1 using different values of relative density. As seen in Fig. 20, the shape of the t-z at 8 m depth is controlled by the shape of the undrained stress-strain curve of the sand. Dr = 30%, 40% and 50% with ε_{50} of 0.8%, 0.65% and 0.55%, respectively, have been used with the 10-m thick liquefiable sand layer Compared to medium dense sands, it can be seen that the rebound of the t-z curve (i.e. soil strength) in loose sands (Dr = 30%) is much slower. Such behavior of loose sands justifies the practice current use of the residual strength of liquefied loose sands.

The change of the PWP induced by different seismic events (i.e. $u_{xs,ff}$ or Δu_c) before the axial load is applied would affect the resulting t-z curve. It should be noted that the change of a_{max} produces different t-z curves at the same depth into the same soil profile as shown in Fig. 21. Using a_{max} less than 0.1g does not yield significant change in the calculated undrained t-z curve. The switch from undrained to drained conditions results in a significant effect on the shape and stiffness of the calculated t-z curve (Fig. 21).

The side resistance of the pile (Q_s) versus pile head settlement is presented in Fig. 22 by utilizing different values of a_{max} with the same M = 5.0 to generate different initial values of r_u in the free-field (i.e. limited liquefaction) before the axial load is applied. The obtained results exhibit the sensitivity of Q_s with respect to small variations in the characteristic of the earthquake. A considerable drop in the pile side resistance can be observed at a_{max} = 0.2g due to the development of full liquefaction. However, less values of a_{max} exhibit a drop in Q_s over the settlement range of z = 4 mm to 12 mm (i.e. design range) for a_{max} < 0.2g. To substitute for the drop in Q_s into the liquefied layer(s), the pile tip and shaft resistance into the non-liquefiable soil layers would provide more resistance but with additional settlement. Figure 22 shows that around 100% increase in the pile axial resistance can be considered in a moderate seismic event (a_{max} = 0.15g and 0.2g) if the soil has been treated in a partially liquefied state instead of being fully liquefied.

During the seismic event the existing pile will be subjected to cycles of loading-unloading mechanism (rocking) (i.e. tensile-compressive or small and large compressive forces for very short periods of time). By the end of the rocking scenario and the development of soil liquefaction (i.e. largest value of r_u), the pile goes back to experience the existing static axial load from the superstructure under new conditions of soil liquefaction. Such a scenario assumes 1) no changes in the properties of the saturated sands around the pile due to the seismic (undrained conditions, constant Dr, no PWP dissipation yet); and 2) the residual shear stress/strain induced by the end of the cyclic loading and beginning of the monotonic loading (the axial load) is zero (i.e. no shear bias)

Case study

Model and full-scale load tests of axially loaded pile in sand with limited liquefaction are very limited. Most tests focus on the combination of lateral and axial loads in fully liquefied soils (r_u = 1) that could damage the pile under bending moment. The full-scale load test performed by Strand (2008) to study the effect of downdrag on piles in liquefied soils is used in its initial phase to study the behavior of axially loaded piles in partially liquefied soils. As observed from reported test data, r_u induced by controlled blasting into the liquefiable sand layer varied with depth (6.7 m to 16.8 m below ground) from 0.9 to 0.1 just immediately after the blast. Table 3 shows the soil profile at the test site 2 and Dr as provided by Strand (2008) based on the CPT data and modified second layer (clay). It should be noted that the PWP dissipated with time and the test results collected immediately after the blast would be employed in the current comparison. As reported by Strand (2008), Piezometers were installed 0.75 m from the center of the pile at depths of 6.7, 8.4, 10.7, 12.8 and 16.8 m below the ground. Strain gauges were installed on the pile every 1.5 m down to 17 m below ground.

A static (pre-blast) load test was carried out one day after the 0.324-m diameter closed-end steel pipe pile was driven approximately 21 m below the ground surface. Figure 23 shows a comparison of measured and computed pile-head load settlement curve collected from the static load test. Good agreement between measured and computed distribution of the axial load carried by the pile shaft down to 17 m below the ground surface is presented in Fig. 24. Significant axial resistance through the second soil layer can be observed in Fig. 24. Compared to other soil layers, the CPT data of the second soil layer showed considerably higher values of friction ratio (R_f) and less q_c Therefore, the second layer is treated in the current analysis as clay layer. The comparison presented in Fig. 25 shows good agreement between measured and calculated t-z curves. Table 3 also presents the values of ε_{50} employed in current analysis. Large depth interval (3.6 m – 15.75 m) is reported with the lowest measured t-z curve (Fig. 25), which is in reasonable agreement with the t-z curve computed at the bottom of the first soil layer. It should be noted that dealing with the second soil layer as clay provides a t-z curve (at 3 m depth) in a very good agreement with the measured one (Fig. 25). Treating the second soil layer as clay yields good agreement with the axial load resistance along the pile in the pre- and post-limited liquefaction case (Figs. 24 and 26). The proposed technique provides the PWP distribution at the soil-pile interface into the liquefiable soil deposit before and after the axial load (365 kN) is applied at the pile head (Fig. 27). The results presented in Fig. 27 consider undrained conditions in the surrounding soil during under the axial loading test.

Summary and Conclusions

The paper presents an approach to predict the behavior of axially loaded piles in partially liquefied and non-liquefied sands. The proposed approach allows the assessment of the load transfer (t–z) and pile head/tip load–settlement curves in sands under drained and undrained conditions. Drained and undrained stress-strain relationships are employed to calculate the pile mobilized side resistance along with the t-z curve with the consideration of developing PWP in surrounding sands. Significant increase in the pile settlement would be anticipated due to the development of partial liquefaction in medium dense sands. The current analysis accounts for the PWP induced by a seismic event and the monotonic axial load applied at the pile head. Pile tip and side resistance are combined in a mobilized fashion to exhibit good comparisons with available field test data using basic pile and soil properties (pile's dimensions and stiffness, and sand's friction angle, relative density, effective unit weight and ε_{50} in addition to M and a_{max} of the earthquake in case of liquefaction potential).

The following conclusions are drawn from the technique presented and related results:

1. The consideration of limited liquefaction in medium dense sand (Dr = 35% - 65%) in the vicinity of axially loaded pile could result in significant cost savings and improvement in the pile axial resistance.

2. The assessment of the full pile-head load – settlement curve in partially liquefied soils allows the designer to capture a representative value of the pile settlement under exiting axial load and associated PWP.
3. The shape of t-z curve in partially liquefied soil is highly influenced by the PWP variation. Therefore, the empirical plot of the t-z curve in liquefiable soil using a reduction factor (a multiplier) could result in unsafe or very conservative design.
4. The wide variation of the medium dense sand properties (Dr = 35% - 65%) should be accounted in the analysis of axially loaded piles in liquefied and non-liquefied sands. Consequently, varying pile responses can be determined for the same category of sands (medium dense).

Acknowledgment

This research was sponsored by the Alabama Department of Transportation (ALDOT Project 930-769)

References

American Association of State Highway and Transportation Officials (AASHTO) (2007). "AASHTO LRFD Bridge Design Specifications." Appendix 10.

Altaee, A., Evigin, E., and Fellenius, B.H. (1992). "Axial load transfer for piles in sand, II. Numerical analysis." Can. Geotech. J., 29(1), 21–29.

Alawneh, A.S., Nusier, O., Malkawi, A.I.H., and Al-Kateeb, M. (2001). "Axial compressive capacity of driven piles in sand: A method including post-driving residual stresses." Can. Geotech. J., 38(2), 364–377.

Ashour, M., and Ardalan, H. (2011). “Piles in Fully Liquefied Soils with Lateral Spread.” Journal of Computers and Geotechnics, 38(5), 821-833.

Ashour, M. and Norris, G.M. (1999). “Liquefaction and undrained response evaluation of sands from drained formulation.” J. Geotech. Geoenviron. Eng., 125(8), 649-658.

Ashour, M., Norris, G. M., and Tung Nguyen (2009). “Assessment of the undrained response of sands under limited and complete liquefaction.” J. Geotech. Geoenviron. Eng., 135(11), 1772-1776.

Ashour, M., and Norris, G., and Pilling, P. (1998). “Lateral loading of a pile in layered soil using the strain wedge model.” J. Geotech. Geoenviron. Eng., 124(4), 303-315.

American Petroleum Institute. Recommended Practice for Planning, Designing and Constructing Fixed Offshore Platforms (1993). “Load and resistance factor design.” API Recommended practice 2A-LRFD, 1st edition.

Bengt, H. Fellenius, and Timothy, C. Siegel. (2008). “Pile drag load and downdrag in a liquefaction event.” J. Geotech. Geoenviron. Eng., 134(9), 1412-1416.

Bhattacharya, S., Bolton, M.D., and Madabhushi, S.P.G. (2005). “A Reconsideration of the safety of the piled bridge foundations in liquefiable soils.” Soils Found., 45(4), 13-25.

Bolton, M.D. (1986). “The strength and dilatancy of sand.” Géotechnique, 36 (1), 65-78.

Castro, G. (1969). “Liquefaction of sands.” Ph.D. thesis, Division of engineering and applied physics, Harvard University, Cambridge.

Chow, Y.K. (1986). “Analysis of vertically loaded pile groups.” Int. J. Numer. Anal. Methods Geomech., 10, 59-72.

Chow, H.S.W. (2007). “Analysis of piled-raft foundations with piles of different lengths and diameters.” PhD thesis, University of Sydney.

Coyle, H.M., and Costello, R.R. (1981). “New design correlations for piles in sand.” J. Geotech. Engrg. Div., 107(7), 965-986.

Coyle, H. M. and Reese, L. C. (1966). “Load Transfer for axially loaded piles in clay.” Journal of Soil Mechanics and Foundations Division, 92(SM2), 1-25.

Elfass, S. (2001). “A new approach for estimating the axial capacity of driven piles in sand up to true soil failure.” Ph.D. thesis, University of Nevada, Reno.

Fellenius, B.H. (1999). “Basics of foundation design. 2nd expanded edition.” BiTech Publishers, Vancouver, 140 p.

Fellenius, B.H. and Siegel, T.C. (2008). “Pile drag load and downdrag in a liquefaction event” Journal of Geotechnical and Geoenvironmental Engineering, 134(9), 1412-1416.

Haldar, S. and Babu, G.L.S. (2010). “failure mechanisms of pile foundations in liquefiable soil: parametric study." International Journal of Geomechanics, 10(2), 74-84.

Hoit, M., McVay, M., and Hays, C. (2007). “FB-MultiPier version 4.11 user’s manual.” Bridge Software Institute, University of Florida, Gainesville, Florida.

Idriss, I. M., and Boulanger, R. W. (2004). “Semi-empirical procedures for evaluating liquefaction potential during earthquakes.” Proc. of the 11th ICSDEE & 3rd ICEGE, 32 – 56.

Jardine, R.J., and Chow, F.C. (1996). “New design methods for offshore piles.” MTD Publication, 96/103, London, Marine Technology Directorate, 48.

Kraft, L.M., Richard, P.R., and Kagawa, T. (1981). “Theoretical t–z curves.” J. Geotech. Engrg. Div., 107(11), 1543–1561.

Maheshwari, B. K. and Sarkar, R. (2011). "Seismic behavior of soil-pile-structure interaction in liquefiable soils: parametric study," International Journal of Geomechanics, 11(4), 335-347.

McVay, M.C., O'Brien, M., Townsend, F.C., Bloomquist, D.G., and Caliendo, J.A. (1989). "Numerical analysis of vertically loaded pile groups." Proc. of Foundation Engineering Congress, ASCE, Northwestern University, Edited by FH Kulhawy, New York, 675–690.

Norris, G.M. (1986). "Theoretically based BEF laterally loaded pile analysis." Proceedings of 3rd International Conference on Numerical Methods in Offshore Piling, Nantes, France, 361-386.

Norris, G.M., Siddharthan, R., Zafir, Z., and Madhu, R. (1997). "Liquefaction and residual strength of sands from drained triaxial tests." J. Geotech. Geoenviron. Eng., 123(3), 220-228.

Randolph, M.F., and Wroth, C.P. (1978). "Analysis of deformation of vertically loaded piles." J. Geotech. Engrg. Div., 104(12), 1465–1488.

Randolph, M.F. (2003). "43rd Rankine lecture: science and empiricism in pile foundation design." Géotechnique, 53(9), 785-796.

Robinsky, E.I., and Morrison, C.E. (1964). "Sand displacement and compaction around model friction piles." Can. Geotech. J., 1(2), 81–93.

Rollins, K.M., and Strand, S.R. (2006). "Downdrag forces due to liquefaction surrounding a pile." Proc. of 8th US Natl. Conf. on Earthq. Engrg., San Francisco, CA, 1646.

Salgado, R., Seo, H., and Prezzi1, M. (2011). "Variational elastic solution for axially loaded piles in multilayered soil." International Journal for Numerical and Analytical Methods in Geomechanics, 35(18), Published online, DOI: 10.1002/nag.1110

Schnertmann, J.H. (1970). "Static cone to compute static settlement over sand." J. Geotech. Engrg. Div., 96(3), 1011–1043.

Schnertmann, J.H., Hartman, J.P., and Brown, P.R. (1978). "Improved strain influence factor diagram." J. Geotech. Engrg. Div., 105(6), 715–726.

Seo, H., Irem, Z.Y., and Prezzi, M. (2009). “Assessment of the axial load response of an H pile driven in multilayered soil.” J. Geotech. Geoenviron. Eng., 135(12), 1789-1804.

Seo, H., Prezzi, M., and Salgado, R. (2008). “Settlement analysis of axially loaded piles.” Proc. of the 6th Int. Conf. on Case Histories in Geotech. Engrg. and Symposium, Arlington, VA.

Seo H., and Prezzi M. (2007). “Analytical solutions for a vertically loaded pile in multilayered soil.” Geomechanics and Geoengineering: An International Journal, 2(1), 51–60.

Shanker, K., Basudhar, P.K., and Patra, N.R. (2007). “Buckling of piles under liquefied soil conditions.” Geotech. Geol. Eng., 25(3), 303-313.

Sonia, A. , and Desai, C.S. (1987). “Load deformation response of axially loaded piles.” J. Geotech. Engrg., 113(12), 1483-1500.

Strand, R.S. (2008). “Liquefaction mitigation using vertical composite drains and liquefaction-induced downdrag on piles: implications for deep foundation design.” Ph.D. thesis, Department of civil and environmental engineering, Brigham young university.

Vaid, Y.P., and Thomas, J. (1995). “Liquefaction and post-liquefaction of behavior of sand.” J. Geotech. Eng., 121(2), 163–173.

Vijayvergiya, V.N. (1977). “Load-movement characteristics of piles.” Proc., Ports 77 Conference, ASCE, Long Beach, CA, 269-286.

Zhu, H., and Chang, F. (2002). “Load transfer curves along bored piles considering modulus degradation.” J. Geotech. Geoenviron. Eng., 128(9), 764–74.

Yao, W, Liu, Y., and Chen, J. (2012) “characteristics of negative skin friction for superlong piles under surcharge loading.” International Journal of Geomechanics, 12(2), 90-97.

Table 1

Table 1. Soil profile

Soil Layer Thick. (m)	Soil Type	Unit Weight, $\overline{\gamma}$ (kN/m^3)	ε_{50} (%)	φ (degree)	^aS_u (kN/m^2)
2.0	Clay	16	2.0	-	20
1.0	Clay	7	2.0	-	20
10.0	Medium dense sand	8	0.8	33	-
5.0	Dense sand	10	0.2	42	-

[a] Undrained shear strength

Table 2

Table 2. Pile head axial load (Q_T) increments

Curve (Load increment) #	1	2	3	4	5	6	7	8	9
Q_T (kN)	130	205	350	400	425	450	530	625	660

Table 3

Table 3. Soil profile at the test site 2 (After Strand 2008)

Soil Layer Thick. (m)	Soil Type	Dr (%) Average	Unit Weight, $\overline{\gamma}$ (kN/m3)	ε_{50} (%)	φ (degree)	S_u (kN/m2
2.8	Medium dense sand	60	18	0.6	34	-
1.5	Stiff clay*	70	8	0.5	28	120
8.5	Medium dense sand	35	7.5	1.0	31	-
6.5	Medium dense sand	50	8	0.8	33	-
3.0	Silt/clayey silt	50	8	2.0	24	20

* Reported as sand silt/silt with the shown Dr and modified in current study to stiff clay

Figure 1

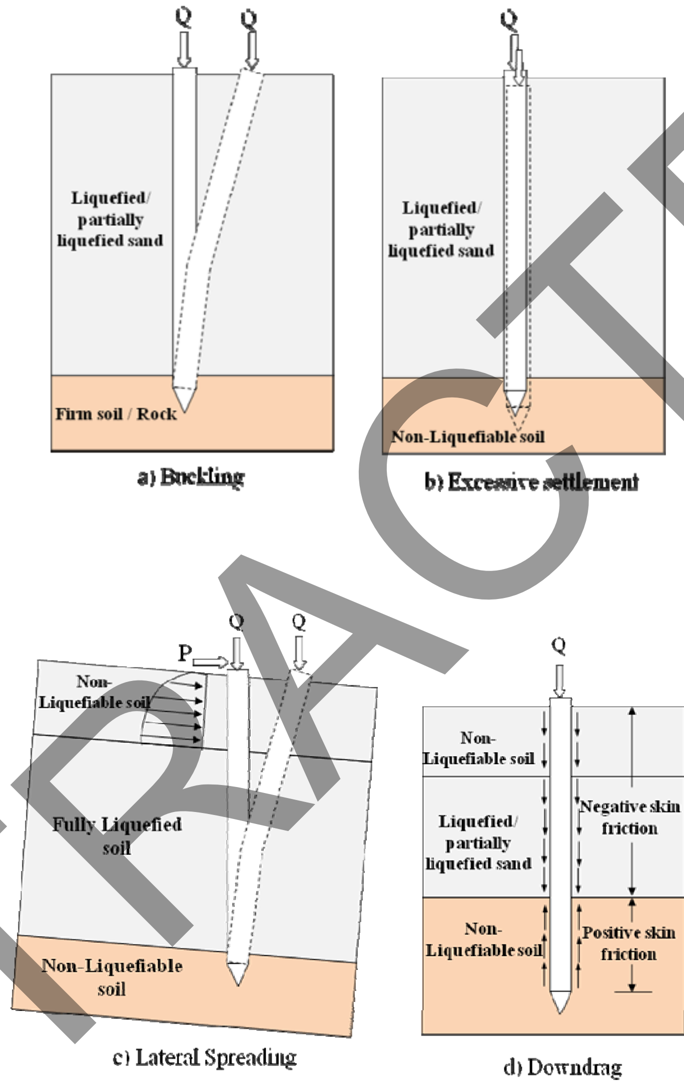

Fig. 1. Different failure modes for a single pile under axial load.

Figure 2

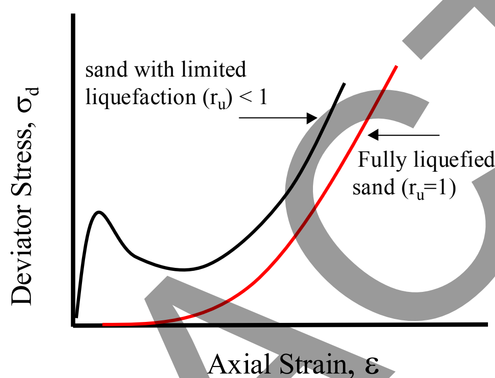

Fig. 2. Variation of near-field strength for fully and limited liquefied sand.

Figure 3

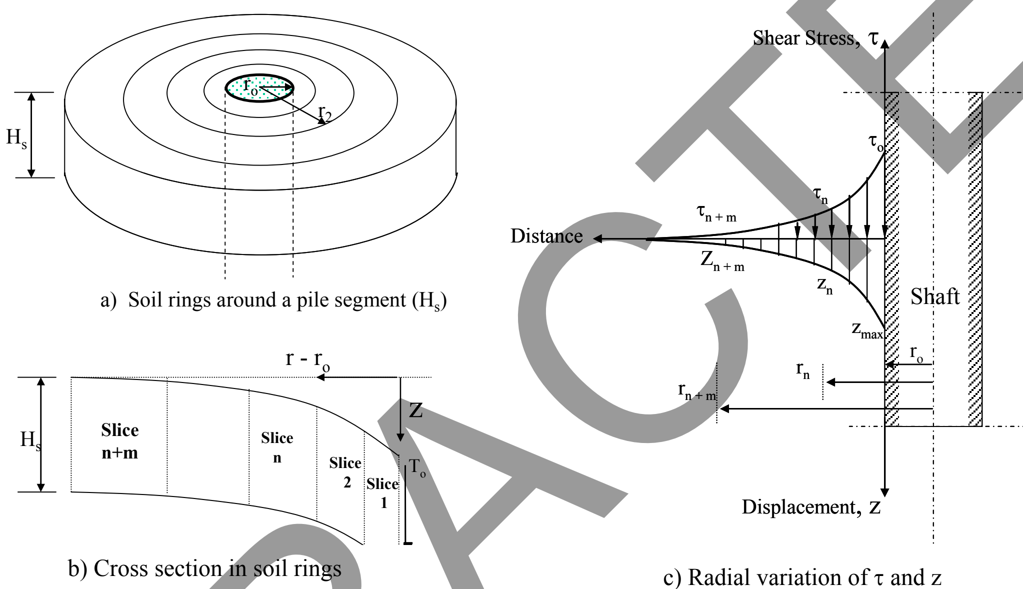

Fig. 3. Modeling sand-pile interaction

Figure 4

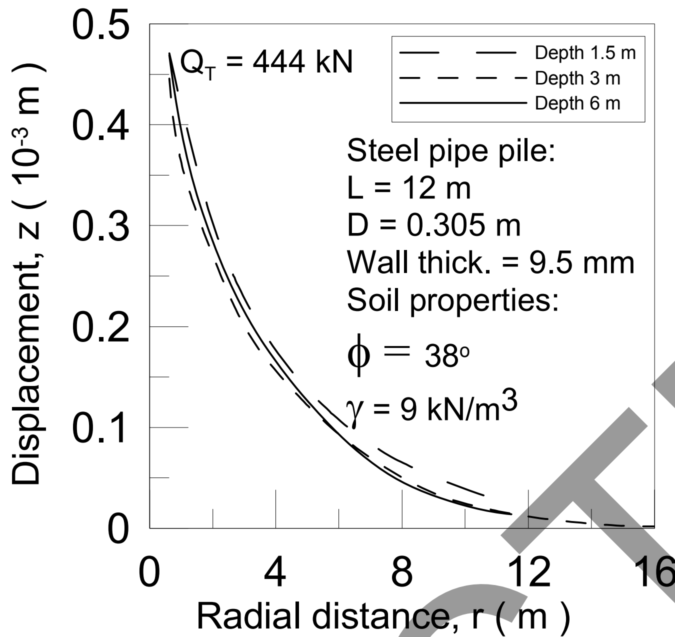

Fig. 4. Radial variation of displacement in the surrounding sand using PLAXIS-3D.

Figure 5

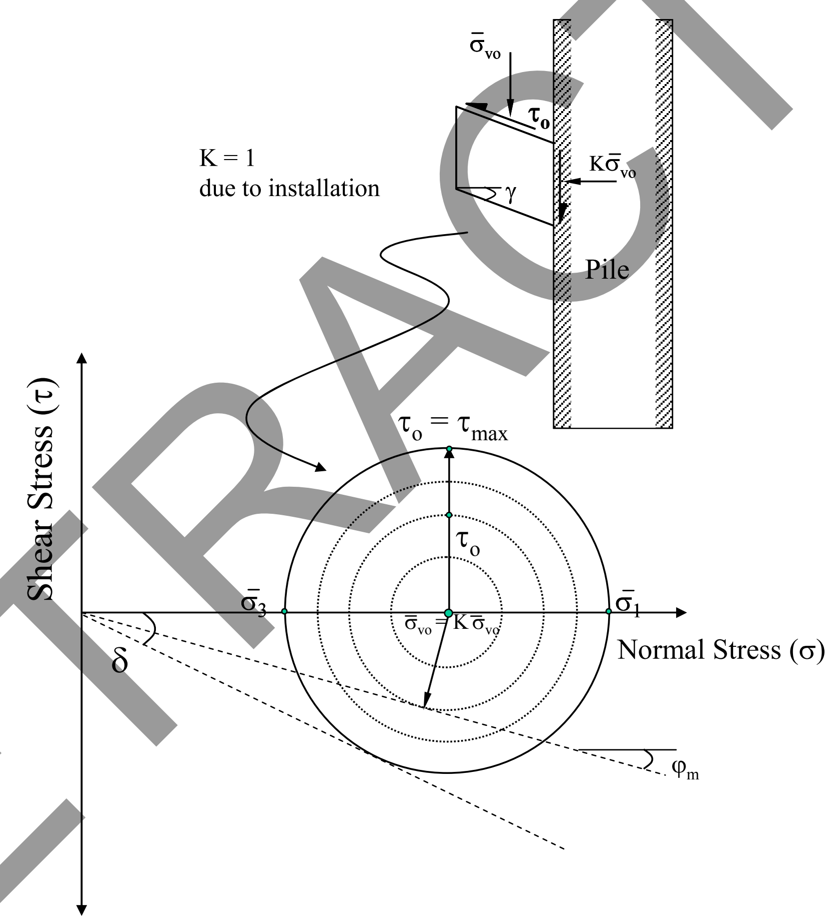

Fig. 5. The progress of shear stress at the soil-pile interface.

Figure 6

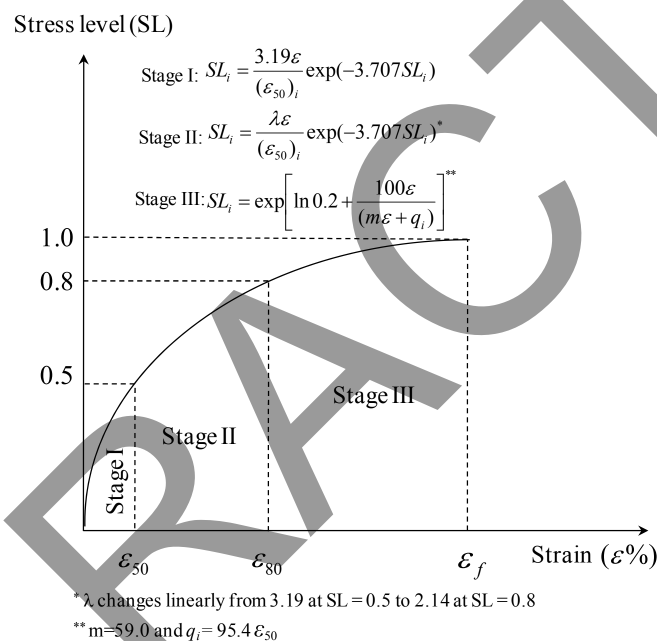

Fig. 6. Stress-strain soil model developed by (After Norris 1985 and Ashour et al. 1998).

Figure 7

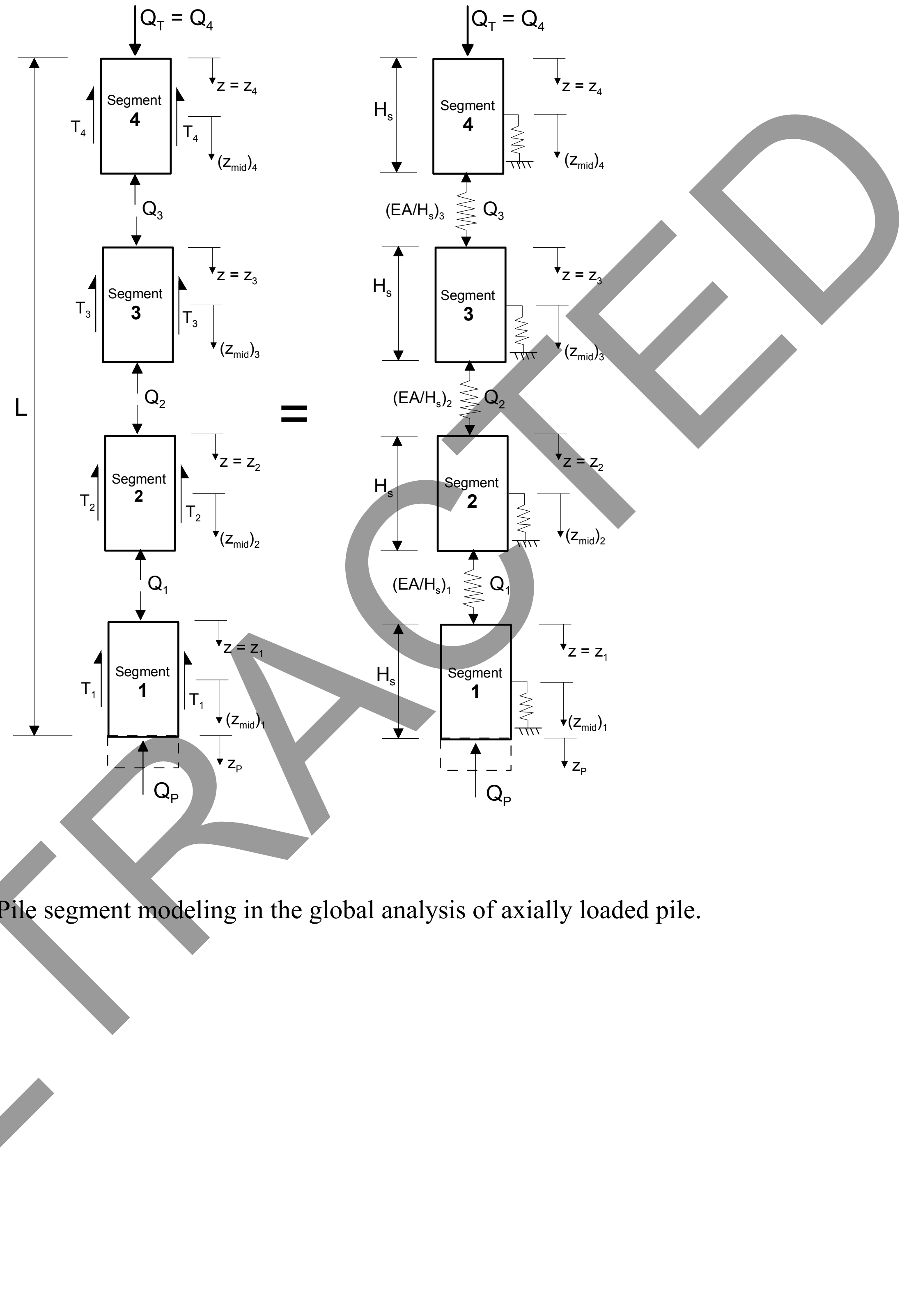

Fig. 7. Pile segment modeling in the global analysis of axially loaded pile.

Figure 8

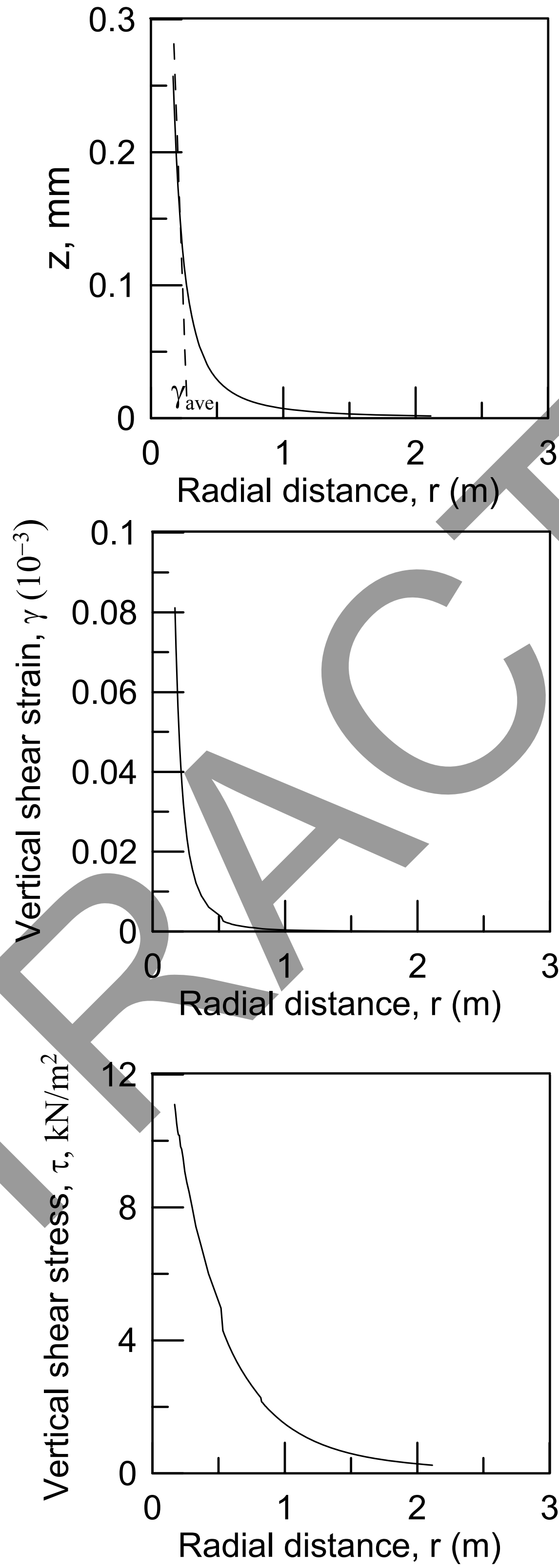

Fig. 8. Radial degradation of displacement and shear stress/strain in sand around the pile

Figure 9

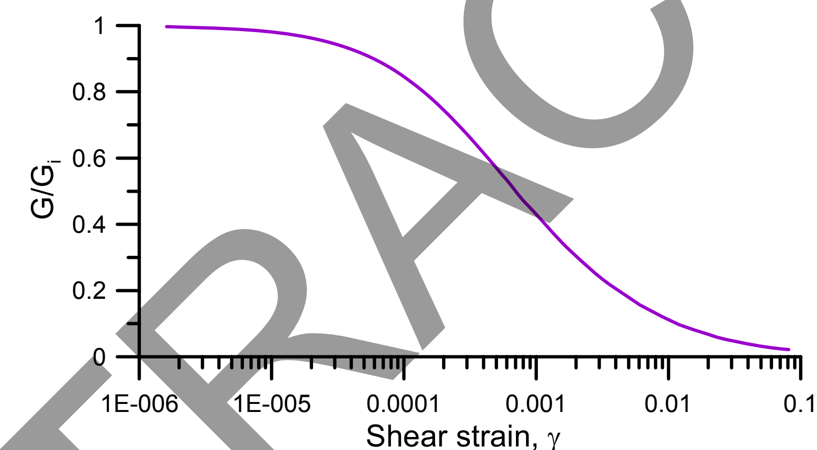

Fig. 9. Shear modulus degradation curve from the utilized soil model.

Figure 10

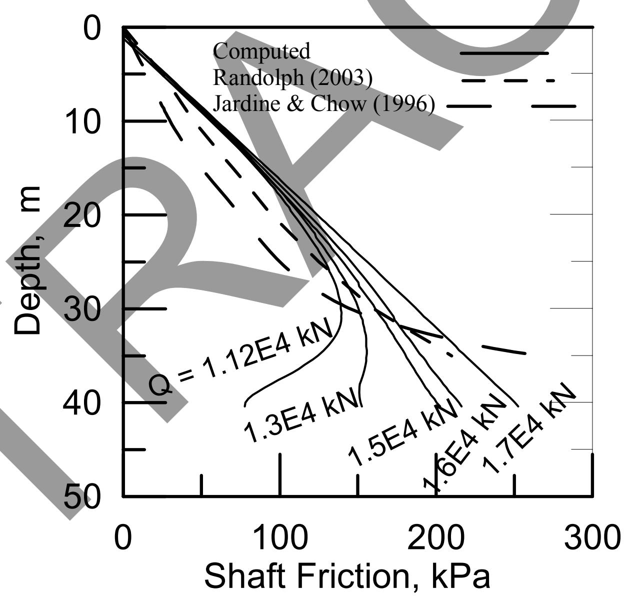

Fig. 10. Computed mobilized soil-pile frictional resistance

Figure 11

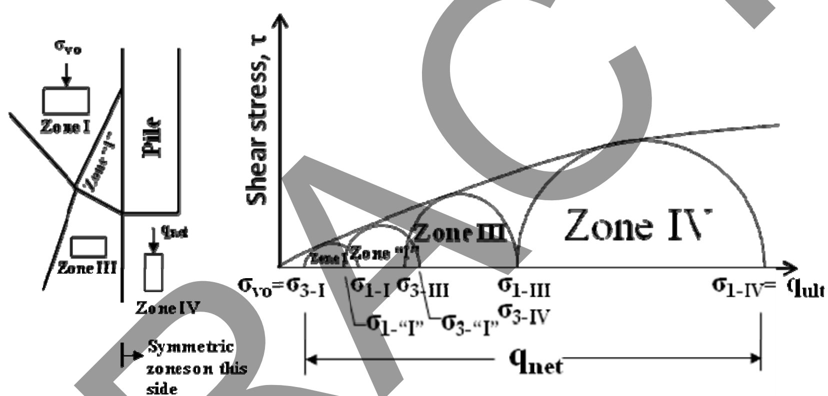

Fig. 11. Degradation in the secant friction angles of circles tangent to a curvilinear envelope of sand due to the increase in the confining pressure (Elfass, 2001).

Figure 12

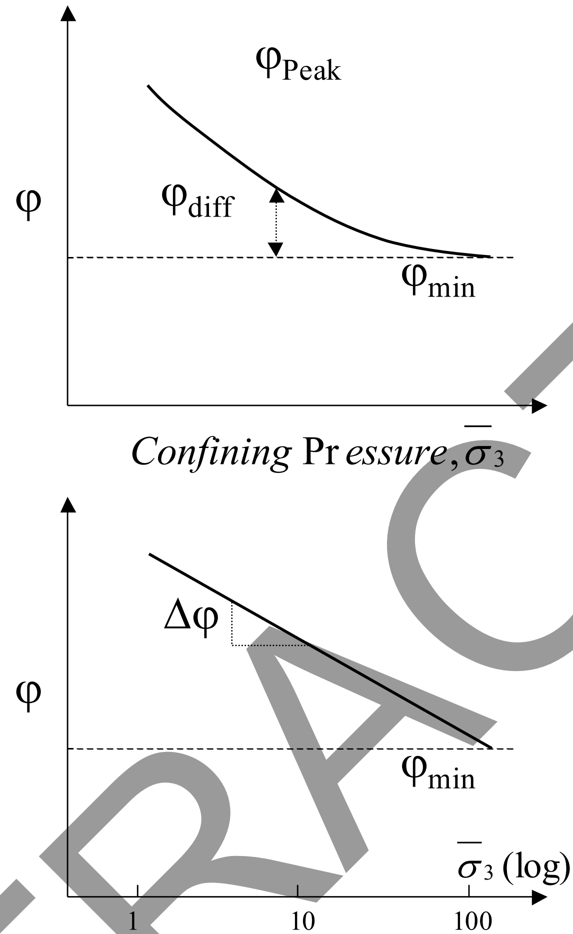

Fig. 12. Changes of Friction Angle (φ) with the Confining Pressure (Ashour et al. 2004).

Figure 13

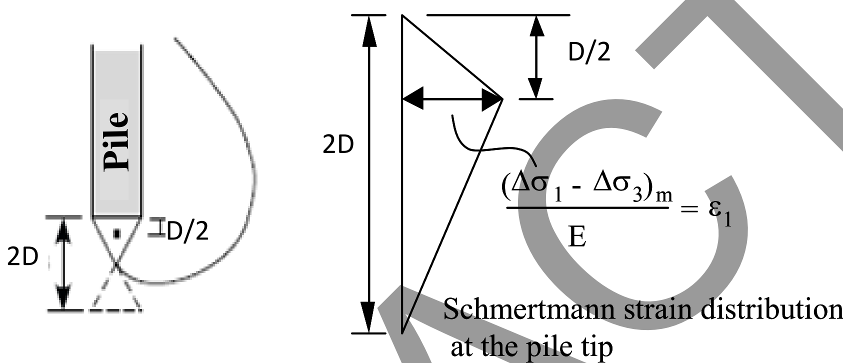

Fig. 13. Strain profile and the associated mobilized stresses immediately below the pile tip, (after Elfass 2001).

Figure 14

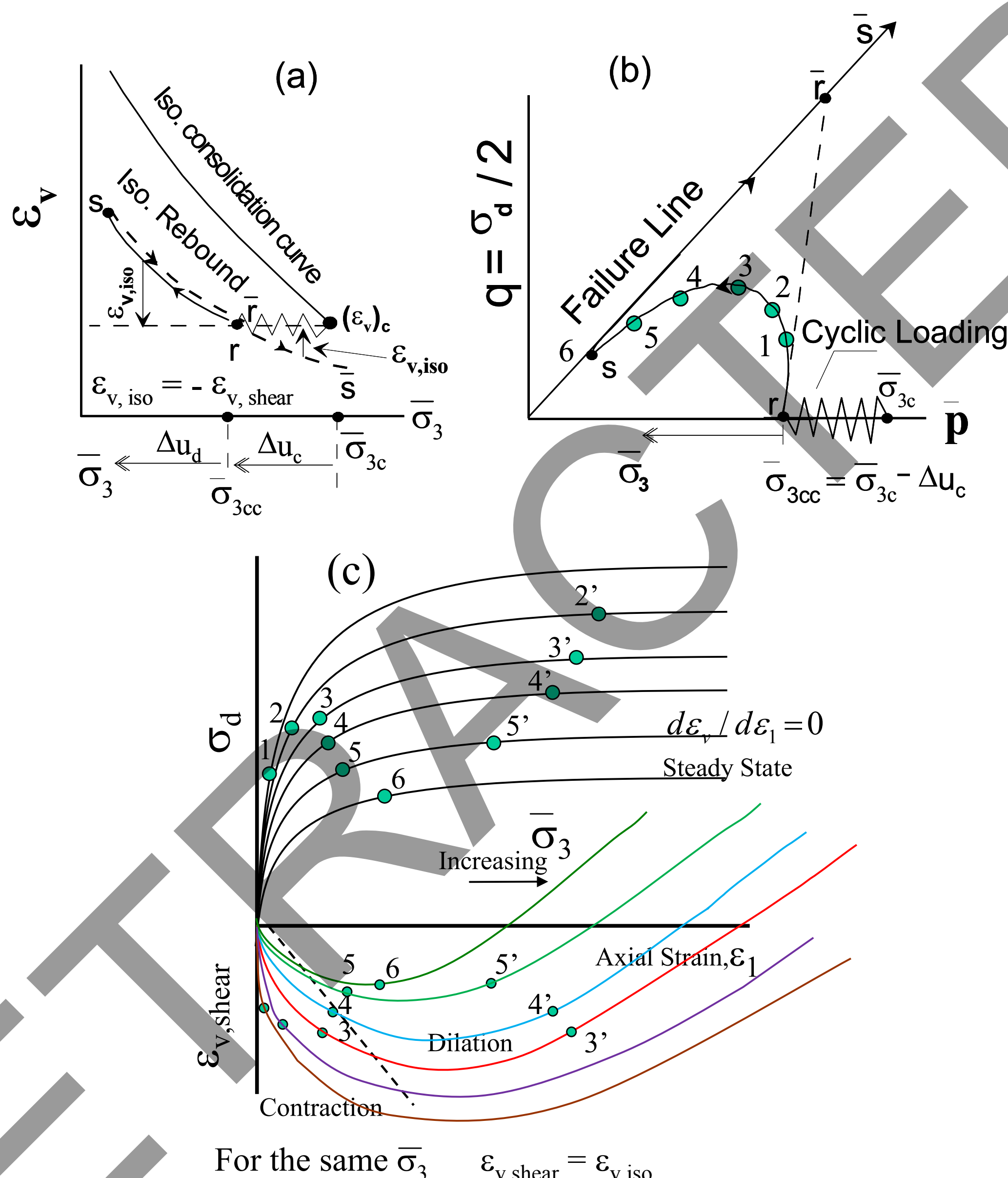

RETRACTED

Fig. 14. Interrelationship among a) isotropic consolidation rebound. b) undrained stress path c) drained and undrained stress-strain behavior

Figure 15

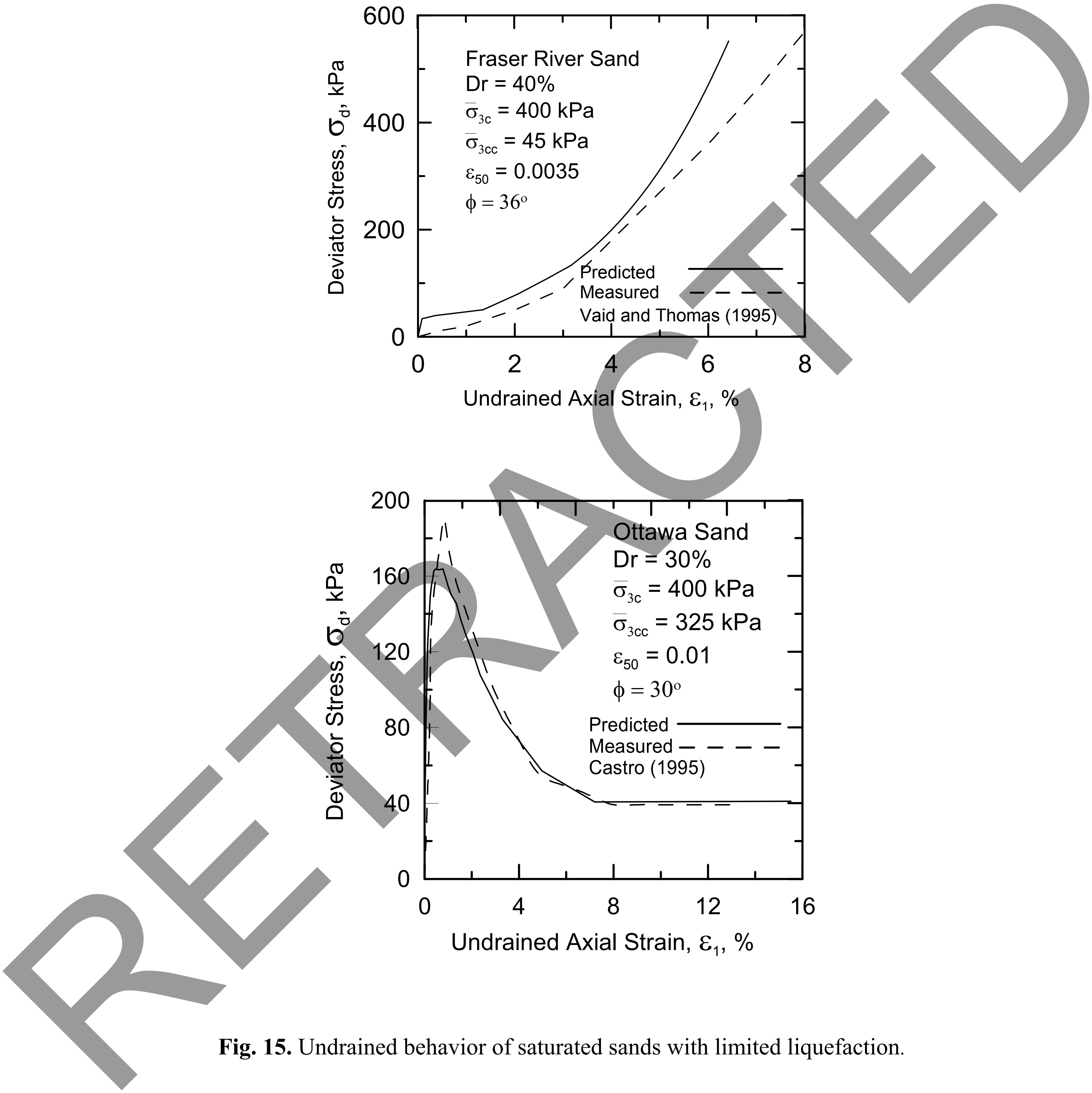

Fig. 15. Undrained behavior of saturated sands with limited liquefaction.

Figure 16

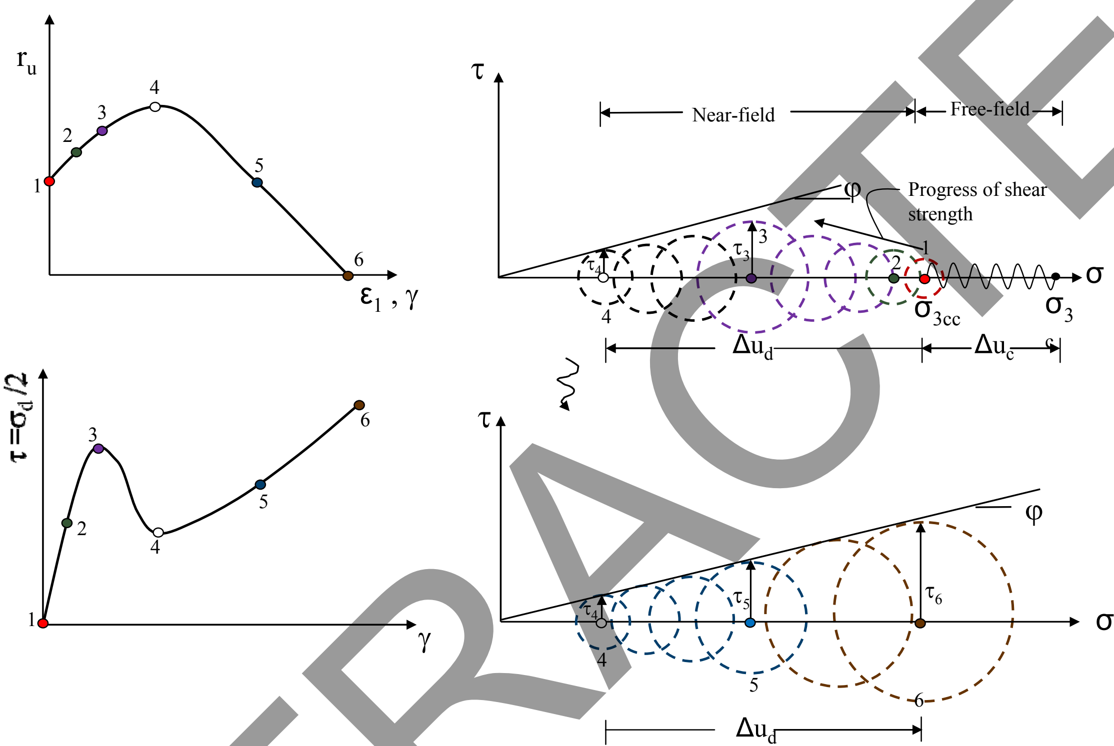

a) Undrained shear strain-strength-PWP variation

b) Post-liquefaction variation of shear strength in the soil-pile interface zone

Fig. 16. Variation of shear strain-strength and water pressure ratio in the partially liquefied sand around the pile.

Figure 17

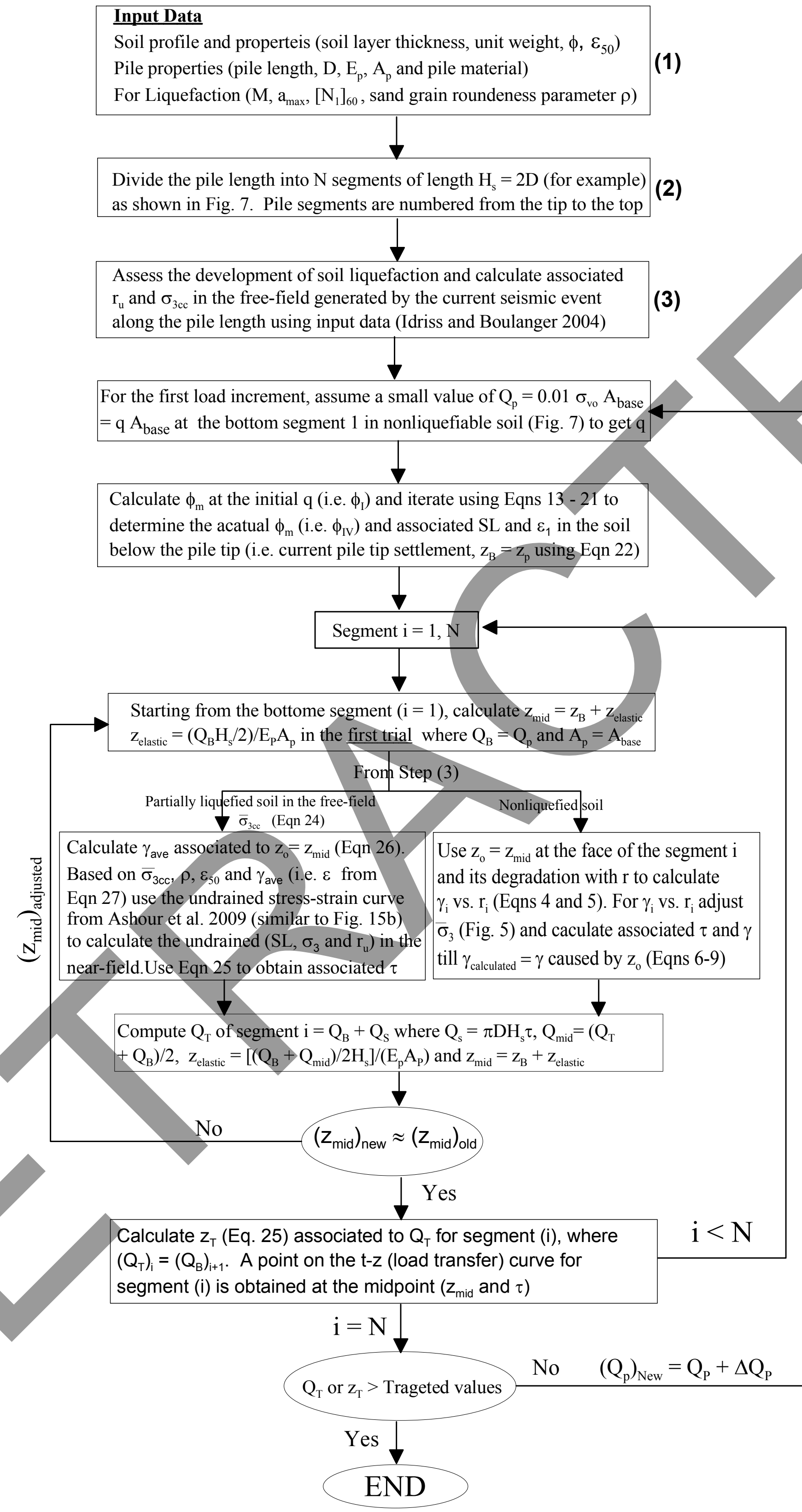

Fig. 17 Flowchart for the calculations of the presented methodology.

Figure 18

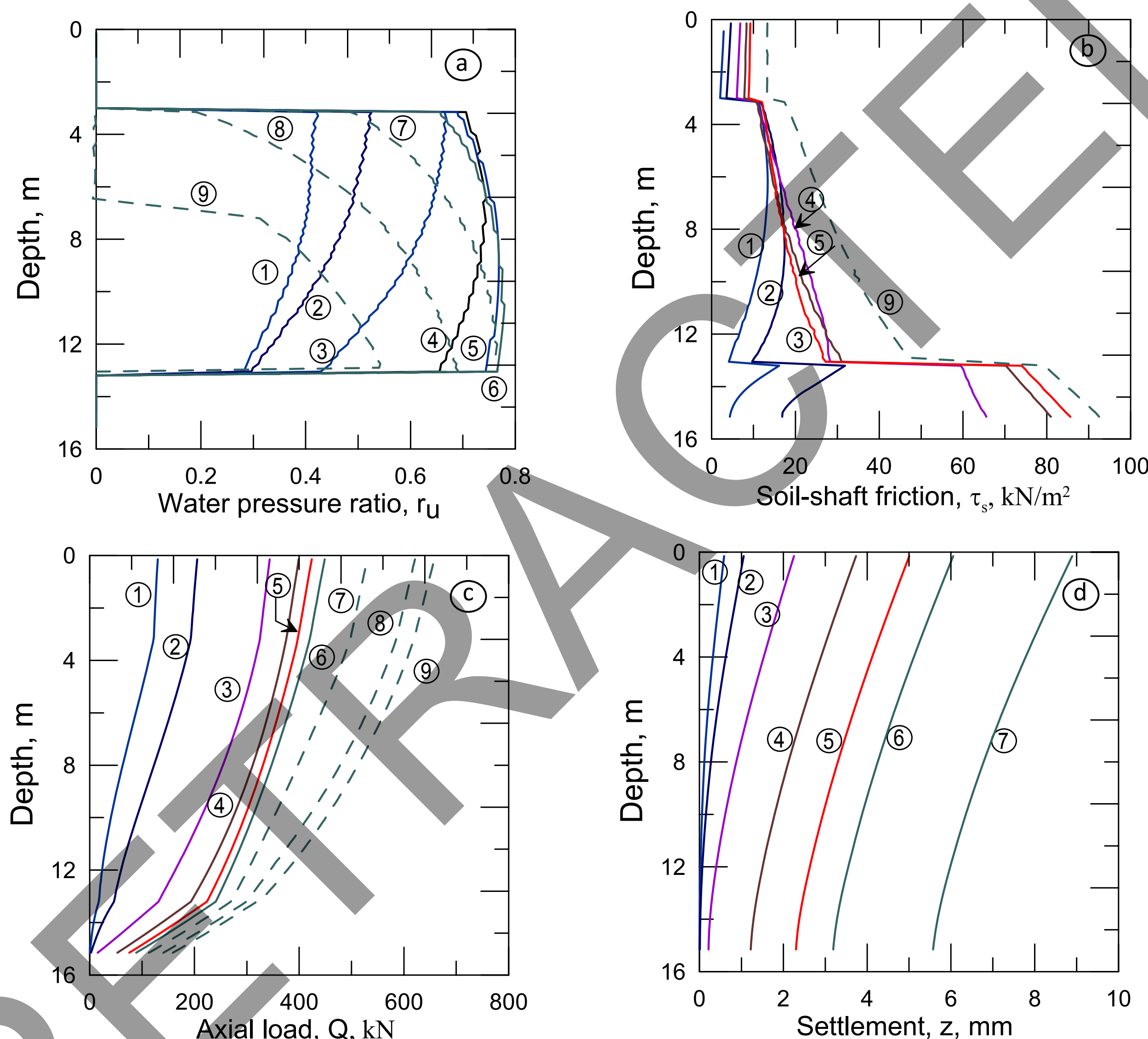

Fig. 18. Variation of r_u, τ_s (or f_s), Q and z under monotonic pile head axial load (Q_T)

Figure 19

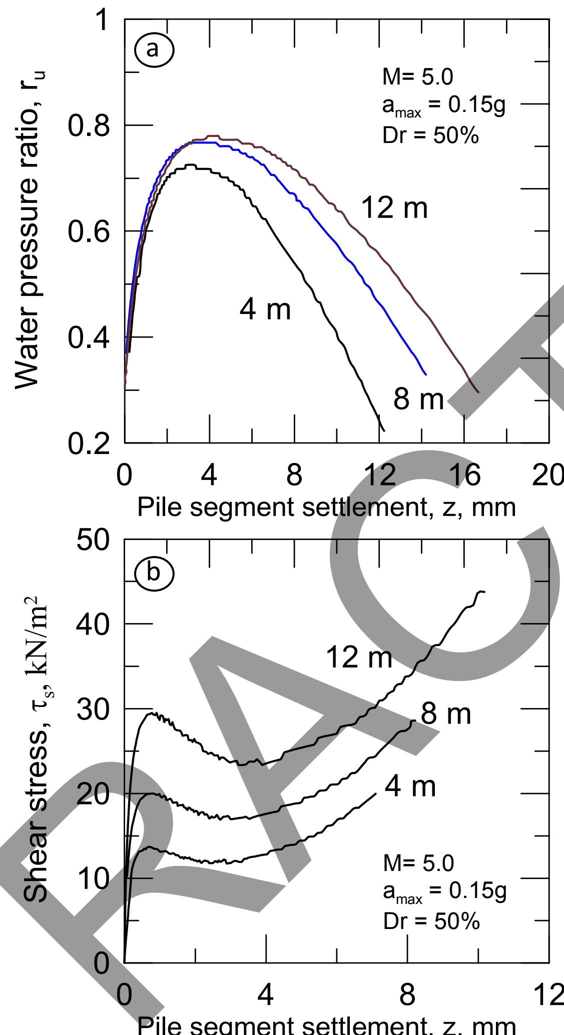

Fig. 19. Variation of r_u, and τ_s versus pile displacement z at different depths.

Figure 20

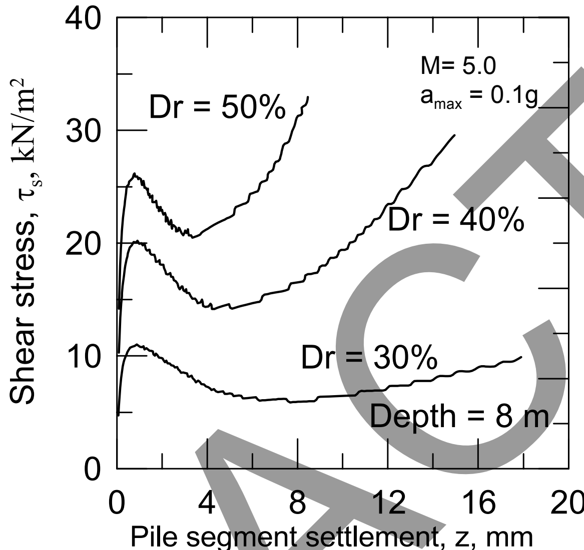

Fig. 20. Effect of Dr of partially liquefied sand on the (t-z) curve shape.

Figure 21

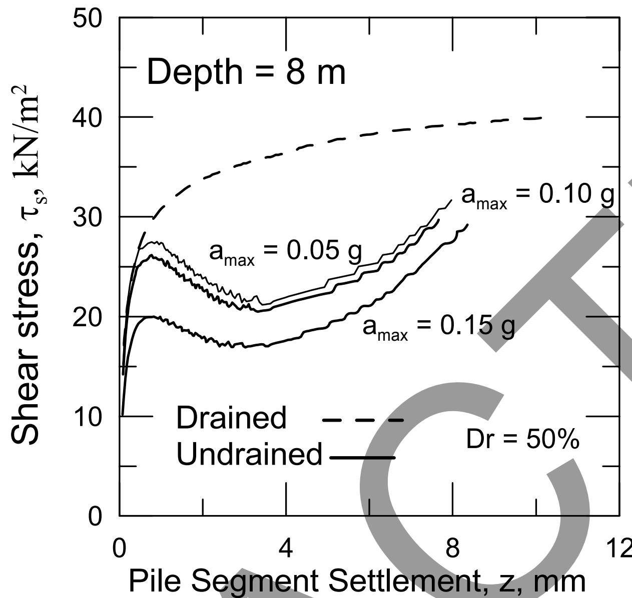

Fig. 21. Effect of a_{max} on the shape of the t-z curve of sand with limited liquefaction.

Figure 22

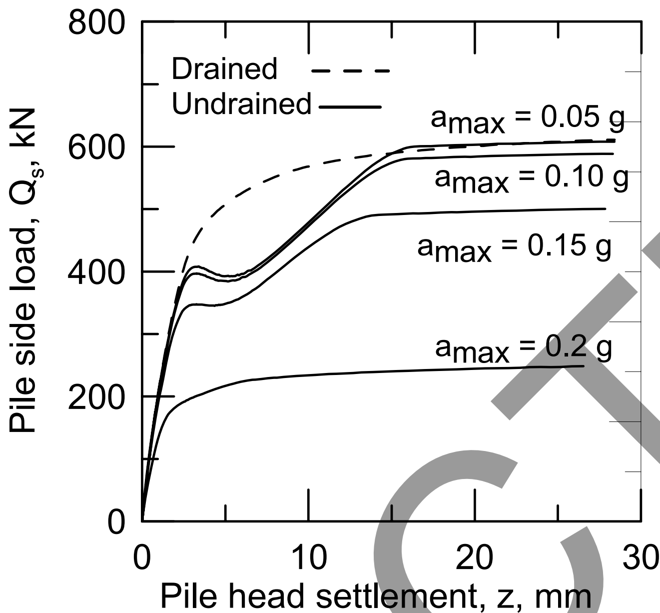

Fig. 22. Effect of a_{max} on the load carried by the pile shaft (Q_s) due to soil liquefaction.

Figure 23

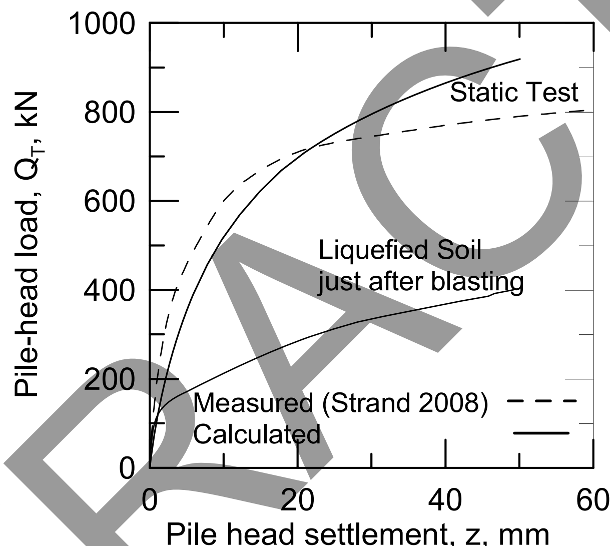

Fig. 23. Comparison of measured and computed pile head load settlement.

Figure 24

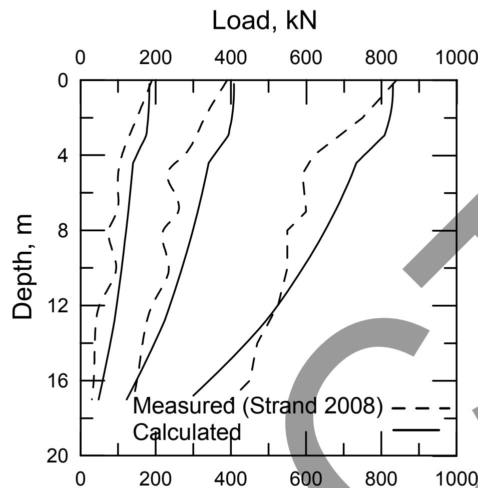

Fig. 24. Measured and computed pre-blasting axial load along the pile.

Figure 25

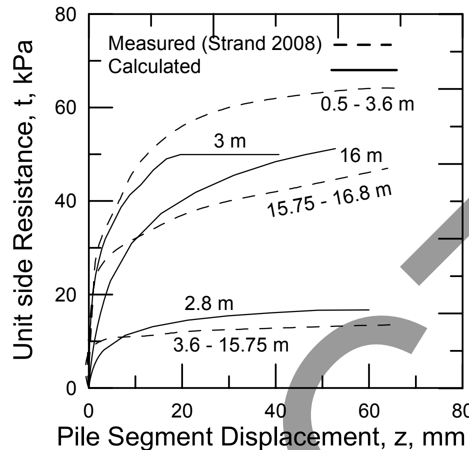

Fig. 25. Comparison of measured and computed static t-z curves.

Figure 26

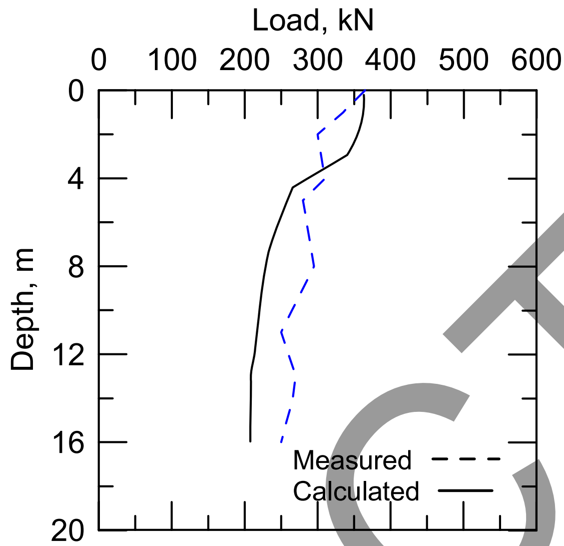

Fig. 26. Measured and computed axial load along the pile immediately after the blast.

Figure 27

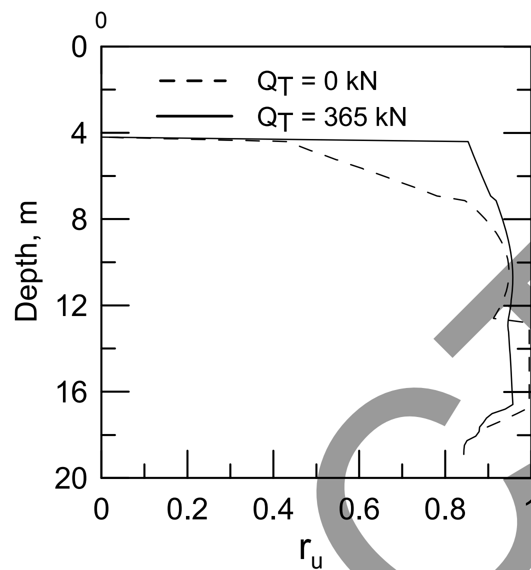

Fig. 27. Computed r_u into the liquefied soil due to axial load after blasting.

Fig. 1. Different failure modes for a single pile under axial load.

Fig. 2. Variation of near-field strength for fully and limited liquefied sand.

Fig. 3. Modeling sand-pile interaction

Fig. 4. Radial variation of displacement in the surrounding sand using PLAXIS-3D.

Fig. 5. The progress of shear stress at the soil-pile interface.

Fig. 6. Stress-strain soil model developed by (After Norris 1985 and Ashour et al. 1998).

Fig. 7. Pile segment modeling in the global analysis of axially loaded pile.

Fig. 8. Radial degradation of displacement and shear stress/strain in sand around the pile

Fig. 9. Shear modulus degradation curve from the utilized soil model.

Fig. 10. Computed mobilized soil-pile frictional resistance

Fig. 11. Degradation in the secant friction angles of circles tangent to a curvilinear envelope of sand due to the increase in the confining pressure (Elfass, 2001).

Fig. 12. Changes of Friction Angle (φ) with the Confining Pressure (Ashour et al. 2004).

Fig. 13. Strain profile and the associated mobilized stresses immediately below the pile tip, (after Elfass 2001).

Fig. 14. Interrelationship among a) isotropic consolidation rebound b) undrained stress path c) drained and undrained stress-strain behavior

Fig. 15. Undrained behavior of saturated sands with limited liquefaction.

Fig. 16. Variation of shear strain-strength and water pressure ratio in the partially liquefied sand around the pile.

Fig. 17 Flowchart for the calculations of the presented methodology.

Fig. 18. Variation of r_u, τ_s (or f_s), Q and z under monotonic pile head axial load (Q_T)

Fig. 19. Variation of r_u, and τ_s versus pile displacement z at different depths.

Fig. 20. Effect of Dr of partially liquefied sand on the (t-z) curve shape.

Fig. 21. Effect of a_{max} on the shape of the t-z curve of sand with limited liquefaction.

Fig. 22. Effect of a_{max} on the load carried by the pile shaft (Q_s) due to soil liquefaction.

Fig. 23. Comparison of measured and computed pile head load settlement.

Fig. 24. Measured and computed pre-blasting axial load along the pile.

Fig. 25. Comparison of measured and computed static t-z curves.

Fig. 26. Measured and computed axial load along the pile immediately after the blast.

Fig. 27. Computed r_u into the liquefied soil due to axial load after blasting.